


RESEARCH

Open Access



# Augmented ERO1 $\alpha$ upon mTORC1 activation induces ferroptosis resistance and tumor progression via upregulation of SLC7A11

Zixi Wang<sup>1,10†</sup>, Huaiyuan Zong<sup>1†</sup>, Weiwei Liu<sup>2†</sup>, Wei Lin<sup>3†</sup>, Anjiang Sun<sup>1</sup>, Zhao Ding<sup>2</sup>, Xu Chen<sup>1</sup>, Xiaofeng Wan<sup>4</sup>, Yanyan Liu<sup>5</sup>, Zhongdong Hu<sup>6</sup>, Hongbing Zhang<sup>7</sup>, Hongwu Li<sup>2,8</sup>, Yehai Liu<sup>2</sup>, Dapeng Li<sup>9\*</sup>, Sumei Zhang<sup>1\*</sup> and Xiaojun Zha<sup>1,9\*</sup> 

## Abstract

**Background** The dysregulated mechanistic target of rapamycin complex 1 (mTORC1) signaling plays a critical role in ferroptosis resistance and tumorigenesis. However, the precise underlying mechanisms still need to be fully understood.

**Methods** Endoplasmic reticulum oxidoreductase 1 alpha (ERO1 $\alpha$ ) expression in mTORC1-activated mouse embryonic fibroblasts, cancer cells, and laryngeal squamous cell carcinoma (LSCC) clinical samples was examined by quantitative real-time PCR (qRT-PCR), western blotting, immunofluorescence (IF), and immunohistochemistry. Extensive in vitro and in vivo experiments were carried out to determine the role of ERO1 $\alpha$  and its downstream target, member 11 of the solute carrier family 7 (SLC7A11), in mTORC1-mediated cell proliferation, angiogenesis, ferroptosis resistance, and tumor growth. The regulatory mechanism of ERO1 $\alpha$  on SLC7A11 was investigated via RNA-sequencing, a cytokine array, an enzyme-linked immunosorbent assay, qRT-PCR, western blotting, IF, a luciferase reporter assay, and a chromatin immunoprecipitation assay. The combined therapeutic effect of ERO1 $\alpha$  inhibition and the ferroptosis inducer imidazole ketone erastin (IKE) on mTORC1-activated cells was evaluated using cell line-derived xenografts, LSCC organoids, and LSCC patient-derived xenograft models.

**Results** ERO1 $\alpha$  is a functional downstream target of mTORC1. Elevated ERO1 $\alpha$  induced ferroptosis resistance and exerted pro-oncogenic roles in mTORC1-activated cells via upregulation of SLC7A11. Mechanically, ERO1 $\alpha$  stimulated the transcription of SLC7A11 by activating the interleukin-6 (IL-6)/signal transducer and activator of transcription 3 (STAT3) pathway. Moreover, ERO1 $\alpha$  inhibition combined with treatment using the ferroptosis inducer IKE exhibited synergistic antitumor effects on mTORC1-activated tumors.

<sup>†</sup>Zixi Wang, Huaiyuan Zong, Weiwei Liu and Wei Lin contributed equally to this work.

\*Correspondence:

Dapeng Li

ldpeagle1@163.com

Sumei Zhang

zhangsume@ahmu.edu.cn

Xiaojun Zha

zhaxiaojunpumc@gmail.com

Full list of author information is available at the end of the article



**Conclusions** The ERO1 $\alpha$ /IL-6/STAT3/SLC7A11 pathway is crucial for mTORC1-mediated ferroptosis resistance and tumor growth, and combining ERO1 $\alpha$  inhibition with ferroptosis inducers is a novel and effective treatment for mTORC1-related tumors.

**Keywords** mTOR, Ferroptosis, ERO1 $\alpha$ , SLC7A11, Tumor growth

## Introduction

The serine/threonine protein kinase mechanistic target of rapamycin (mTOR) is essential for regulating the fundamental biological processes of cell growth and survival [1]. mTOR signaling is mediated by two branches, mTOR complex 1 (mTORC1) and mTOR complex 2 (mTORC2), which are different in terms of specific binding partners, upstream and downstream signaling, and the response to rapamycin [2]. mTORC1 regulates several biological processes important for cell growth and metabolism by integrating numerous signals such as growth factors, amino acids, and energy sources [3, 4]. The tuberous sclerosis 1 (TSC1)/tuberous sclerosis 2 (TSC2) complex is a well-known upstream suppressor of mTORC1 signaling [5]. Depending on the GTPase activity of TSC2, the TSC1/TSC2 complex inhibits the Ras homolog enriched in the brain (Rheb), a small GTPase, by promoting the conversion of active Rheb-GTP to inactive Rheb-GDP [6]. Dissociation of the TSC1/TSC2 complex by inactivating mutations in either *TSC1* or *TSC2* genes or by the phosphorylation of TSC2 with protein kinase B (AKT) results in the accumulation of Rheb-GTP, which ultimately switches on mTORC1 signaling [7]. mTORC1 enhances protein synthesis primarily via the phosphorylation of two key downstream effectors, ribosomal protein S6 kinase 1 (S6K1) and eukaryotic translation initiation factor 4E-binding protein 1 (4E-BP1), and then promotes cell growth and proliferation [1]. Accumulating evidence indicates that mTORC1 signaling is frequently over-activated in human cancers [8, 9], but the precise mechanisms still require further elucidation.

Ferroptosis is a recently identified type of cell death driven by iron-dependent lipid peroxidation [10]. In terms of morphology, its typical manifestations include increased mitochondrial membrane density, a significant reduction of cristae, and mitochondrial shrinkage [10]. Lipid peroxidation is the core reaction of ferroptosis, which is a process that leads to oxidative degradation of lipids, resulting in the formation of peroxide and hydroperoxide derivatives [11]. The main primary products of lipid peroxidation are lipid hydroperoxides. Among the secondary products of lipid peroxidation, malondialdehyde (MDA) is believed to be the most mutagenic product, whereas 4-hydroxynonenal (4-HNE) is the most toxic [12]. Several ferroptosis defense systems have been found in cells to maintain

cell survival by counteracting the adverse effects of lipid peroxidation [10, 13]. The glutathione peroxidase 4 (GPX4)/Glutathione (GSH) system is the primary cellular defense against ferroptosis [14]. Member 11 of the solute carrier family 7 (SLC7A11), an upstream molecule of the GPX4/GSH system, plays a vital role in resisting ferroptosis [15]. It mediates the intake of cystine, which is then reduced to cysteine within the cell and participates in GSH synthesis [15]. GPX4 specifically catalyzes the loss of oxidative activity of lipid peroxides in a GSH-dependent manner, thereby inhibiting ferroptosis [16]. Compounds such as erastin (an inhibitor of SLC7A11) or RAS-selective lethal 3 (RSL3, a GPX4 inhibitor) can induce ferroptosis, while antioxidants, such as ferrostatin-1 and liproxstatin-1 (Lip-1), can suppress ferroptosis [17]. A growing amount of preclinical evidence suggests that inducing ferroptosis is an effective way to treat tumors [18, 19].

Recently, mTORC1 was found to act as a negative regulator of ferroptosis in cancer cells [20]. For example, Zhang et al. reported that cyst(e)ine promotes GPX4 protein synthesis by activating mTORC1 signaling, thus enhancing ferroptosis resistance to RSL3 [21]. It has also been reported that mTORC1 promotes de novo monounsaturated fatty acid synthesis and ferroptosis resistance by upregulating the sterol regulatory element-binding protein 1/stearoyl-CoA desaturase 1 axis [22]. Nevertheless, the exact mechanisms by which mTORC1 promotes ferroptosis resistance remain largely uncharacterized.

In this study, by analyzing mTORC1-activated mouse embryonic fibroblasts (MEFs) and cancer cells, laryngeal squamous cell carcinoma (LSCC) clinical samples, LSCC patient-derived organoids (PDO), and LSCC patient-derived xenograft (PDX) models, we established that endoplasmic reticulum oxidoreductase 1 alpha (ERO1 $\alpha$ ) is involved in hyperactivated mTORC1-mediated ferroptosis resistance and tumor growth. We also demonstrated that ERO1 $\alpha$  upregulates SLC7A11 by activating the interleukin-6 (IL-6)/signal transducer and activator of transcription 3 (STAT3) pathway, thus promoting ferroptosis resistance and tumoral growth of mTORC1-activated cells. Moreover, we showed that ERO1 $\alpha$  inhibition sensitizes mTORC1-activated cells or tumors to the ferroptosis inducer imidazole ketone erastin (IKE). We posit that the ERO1 $\alpha$ /IL-6/STAT3/

SLC7A11 pathway is critical for mTORC1-mediated ferroptosis resistance and tumor growth and that it can be targeted for the treatment of cancers associated with dysregulated mTORC1 signaling.

## Materials and methods

### Reagents and antibodies

Rapamycin (a mTORC1 specific inhibitor), MHY1485 (a mTOR activator), S3I-201 (a selective STAT3 inhibitor), IKE, and Lip-1 were purchased from Selleck Chemicals (TX, USA). Puromycin and deferoxamine (DFX) were sourced from Sigma-Aldrich (MO, USA). Erastin, recombinant mouse IL-6, monokine induced by interferon-gamma (MIG), and macrophage inflammatory protein-1 alpha (MIP-1 $\alpha$ ) proteins were obtained from Med Chem Express (NJ, USA). Plasmids such as pBabe-puro, pBabe-puro-STAT3C (constitutively activated STAT3), pGL3-Basic, and pRL-TK were previously reported [23]. Lenti-CRISPRv2, pMD2.G, and psPAX2 plasmids were obtained from Addgene (MA, USA). The antibodies used in this article were listed in Supplementary Table S1.

### Cell lines and cell culture

All MEF cell lines (Tsc1+/+, Tsc1-/-, Tsc2+/+, and Tsc2-/-) have been described previously [23, 24]. The human umbilical vein endothelial cells (HUVECs), human embryonic kidney 293 T (HEK 293 T) cells, human pancreatic carcinoma cells (PANC-1), human breast carcinoma cells (MDA-MB-231), human lung adenocarcinoma cells (A549), and human cervical cancer cells (HeLa) were obtained from the American Type Culture Collection (VA, USA). LSCC cell lines (Raptor-knockdown LIU-LSC-1 cells, TSC2-knockout TU177 cells, and their respective controls) were described in a previous study [25]. MEFs, HUVECs, HEK 293 T, PANC-1, MDA-MB-231, A549, and HeLa cells were cultured in DMEM Medium (BOSTER, Wuhan, China) supplemented with 10% fetal bovine serum (Gibco, CA, USA) and 1% penicillin-streptomycin (Beyotime, Jiangsu, China). LSCC cell lines were cultured in RPMI 1640 medium (BOSTER) with the same composition as MEFs. Cell cultures were frequently monitored for mycoplasma contamination, and only mycoplasma-negative cells were used for experiments.

### Clinical specimens

LSCC tissues and adjacent normal mucosal (ANM) tissues were collected from the First Affiliated Hospital of Anhui Medical University during 2021 to 2022 with patient consent. Prior to surgery, all recruited patients had not undergone chemotherapy, radiotherapy, or any other antitumor therapies. Histological diagnosis of LSCC was confirmed by at least two experienced

pathologists for all samples. The use of tissue samples in this study was approved by the Research Ethics Committee of the First Affiliated Hospital of Anhui Medical University. Detailed patient information was provided in Supplementary Table S2.

### Establishment of NTC/T1 null cells

A subcutaneous tumor, formed by the injection of Tsc1-/- MEFs into BALB/c-nude mice (GemPharmatech, Nanjing, China), was isolated and immediately washed with cold phosphate-buffered saline (PBS) for 3 times. Subsequently, the tumor tissue was cut into small pieces, and then the small tumor masses were enzymatically dissociated with DMEM medium containing 200 U/ml type IV collagenase (Sigma-Aldrich) at 37 °C for 12 h. Afterward, the cells were washed with PBS and centrifuged, and the sediments were seeded into 6 cm petri dishes and cultured in DMEM medium containing 10% fetal bovine serum (Gibco). Cells were passaged every 3–4 days to prevent cell confluency. Cancer-associated fibroblasts were removed by brief exposure to a 0.25% trypsin solution (Beyotime). This newly established cell line was named NTC/T1 null, and the deletion status of TSC1 in the cells was confirmed by western blotting.

### Generation of a ERO1 $\alpha$ knockout (KO) cell line using CRISPR-Cas9

Ero1 $\alpha$  KO NTC/T1 null cell lines were generated following a protocol from the Feng Zhang lab (<https://zhanglab.bio>) using Lenti-CRISPRv2 plasmids. The sgRNA target sequence for Ero1 $\alpha$  was 5'-GTAGTTAT'TAAACTTATCGA-3'. Lentivirus was produced by co-transfecting the recombinant viral plasmids with packaging vectors (pMD2.G and psPAX2) into HEK 293 T cells. The virus-containing supernatant was harvested 48 h after transfection and infected with NTC/T1 null cells, followed by selection with puromycin for 1 week. Then, the cells were trypsinized, diluted to single cells, and seeded into 96-well plates. Positive single clones were identified by western blotting. An empty Lenti-CRISPRv2 vector was used to generate a control cell line.

### Lentivirus production and transduction

All of the lentiviral vectors were provided by GenePharma (Shanghai, China), which included the LV4 lentiviral plasmid expressing ERO1 $\alpha$  cDNA, SLC7A11 cDNA, and the empty plasmid; LV-2N lentiviral shRNA expression vector targeting ERO1 $\alpha$ , SLC7A11, and the control scrambled shRNA (shSc). The detailed information of the target sequences was listed in Supplementary Table S3. Lentivirus production and the generation of stable cell lines have been described previously [23].

### Western blotting

Western blotting was performed as described previously [26]. In brief, cell or tissue lysates were separated using NuPAGE 4–12% Bis–Tris gels (Life Technologies, CA, USA) and subsequently transferred onto PVDF membranes (Millipore, MA, USA). Following blocking with 5% skim milk, the membranes were incubated with primary and secondary antibodies. Finally, the protein bands were visualized using Pierce™ ECL Western Blotting Substrate (Thermo Fisher Scientific, MA, USA) with a ChemiScope 6100 instrument (Clinx, Shanghai, China).

### Quantitative real-time PCR (qRT–PCR)

Total RNA was extracted from cultured cells using TRIzol reagent (Invitrogen, CA, USA) following the manufacturer's instructions. The quality and concentration of the extracted RNA were assessed using NanoDrop 2000 (Thermo Fisher Scientific). 1 µg of total RNA was transcribed into first-strand cDNA using a RevertAid™ First Stand cDNA Synthesis Kit (Fermentas, MA, USA). qRT–PCR was performed using SYBR Premix Ex Taq™ II (TaKaRa, Kyoto, Japan) in qPCR system LightCycler® 96 (Roche, Switzerland) according to the manufacturer's protocol. Expression levels of the target genes were normalized to β-actin using the  $2^{-\Delta\Delta C_t}$  formula. The primer sequences were provided in Supplementary Table S4.

### RNA interference

All siRNA oligonucleotides were synthesized by GenePharma. Cells were transfected with siRNA at a confluence of 50–60% using GP-transfect-mate (GenePharma) according to the manufacturer's protocol. The target sequences were provided in Supplementary Table S5.

### Tsc2 +/– mice

Tsc2 +/– mice were described previously and backcrossed to Balb/c strain for over 10 times [27]. Toes were used for DNA extraction and genotyping. Kidneys were collected from ten-month-old mice upon sacrifice for subsequent immunohistochemistry analysis.

### Reporter constructs and luciferase reporter assay

The genomic region containing the mouse *SLC7A11* promoter (–575 to +144) was amplified by PCR and then cloned into the pGL3-Basic vector to construct the *SLC7A11* promoter luciferase reporter. Potential STAT3 binding sites within the promoter of the mouse *SLC7A11* gene were mutated using the Q5 Site-Directed Mutagenesis Kit (NEB, MA, USA). Primers sequences were listed in Supplementary Table S6.

To determine the impact of STAT3 on the transcription of *SLC7A11*, HEK 293T cells were seeded in 24-well plates and co-transfected with wild-type or mutated

promoter constructs (200 ng), along with pBabe-puro-STAT3C (200 ng) or the empty vector pBabe-puro and the internal control pRL-TK (10 ng). Luciferase activity was analyzed using the Dual-Luciferase Reporter Assay System (Promega, WI, USA) following the manufacturer's protocol. Relative luciferase activity was normalized to the Renilla luciferase internal control.

### Immunofluorescence (IF) staining

Cells ( $2 \times 10^4$ ) were seeded in 35 mm glass bottom culture dishes (Thermo Fisher Scientific) and incubated overnight. After fixed with 4% paraformaldehyde, permeabilized with 0.1% Triton X-100, and blocking with 3% bovine serum albumin, the cells were stained with primary antibodies overnight at 4 °C, followed by incubation with Alexa Fluor 647-conjugated or CY3-conjugated secondary antibodies (Beyotime) for 1 h. The dishes were counterstained for cell nuclei with DAPI (Beyotime). Fluorescent images were acquired using an LSM880 + Airyscan confocal laser scanning microscope (Carl Zeiss, Oberkochen, Germany).

### Transmission electron microscopy (TEM) assay

Cells were seeded in 10 cm dishes and treated with erastin for 16 h. After washing with cold PBS, the cells were fixed with 2.5% glutaraldehyde in phosphoric acid buffer for 2 h, followed by additional fixation in 1% osmium tetroxide for 2 h. And then, cell sections were dehydrated in ethanol and embedded in acetone. The sections, with a thickness of 70 nm, were stained with uranium acetate and lead citrate. TEM images were captured using the transmission electron microscope (JEOL, Tokyo, Japan).

### MDA assay

The level of MDA was determined using a Lipid Peroxidation MDA Assay Kit (Beyotime). In brief, cells were plated at approximately 80% confluency into 6 cm dishes. After pre-treatment with erastin for 24 h, the cells were lysed, and the supernatant was collected following centrifugation. Tumor tissues were homogenized and sonicated in RIPA buffer (Beyotime) on ice, and then the supernatant was collected by centrifuging at  $12,000 \times g$  for 15 min at 4 °C. Protein concentrations of the cell and tissue lysates were measured using a BCA Protein Assay Kit (Beyotime). MDA levels in the collected cell and tissue supernatant were measured following the manufacturer's instructions.

### L-ROS assay

Cells were seeded at a density of 60–70% confluence into 6-well plates. After treatment with erastin for 24 h, the cells were stained with 2 µM C11 BODIPY (581/591) (Thermo Fisher Scientific) for 25 min at 37 °C.



Subsequently, the cells were washed, trypsinized, and resuspended in 300  $\mu$ l fresh PBS. Next, the cells were passed through a 40- $\mu$ m cell strainer and analyzed with a flow cytometer (Beckman Coulter, CA, USA). Oxidation of BODIPY C11 resulted in a shift of the fluorescence emission peak from 590 to 510 nm. Data was analyzed using Cytobank (<https://www.cytobank.cn/>).

#### GSH assay

A total of  $1 \times 10^6$  cells were seeded into 6 cm culture dishes. After treatment with erastin for 24 h, the cells were harvested for the quantification of GSH and GSSG using a GSH and GSSG Assay Kit (Beyotime) according to the manufacturer's protocol. The total GSH and GSSG levels were calculated using a standard curve and normalized to the total protein content, determined using the BCA method. The following formula: reduced GSH = total glutathione (GSH + GSSG) - GSSG  $\times$  2, was used to calculate the concentration of reduced GSH.

#### Chromatin immunoprecipitation (ChIP)

A ChIP assay was conducted using a SimpleChIP<sup>®</sup> Plus Enzymatic Chromatin IP kit (Cell Signaling Technology, MA, USA) according to the protocol provided by the manufacturer. In brief, cells were crosslinked with 1% formaldehyde, and chromatin was extracted and sonicated to an average size of 200–500 bp using an Ultrasonic crusher (Thermo Fisher Scientific). Subsequently, the samples were incubated with an anti-STAT3 Tyr<sup>705</sup> antibody (Cell Signaling Technology) overnight at 4 °C. The immunoprecipitated DNA was purified and analyzed by PCR or qRT-PCR using specific primers. The primer sequences were listed in Supplementary Table S7.

#### Cell viability, EdU staining and Colony formation assays

Cell proliferation was evaluated using the Cell Counting Kit-8 (CCK-8) kit (Beyotime). Cells were seeded onto 96-well plates at  $2 \times 10^3$  cells/well density. The 10  $\mu$ L of CCK-8 solution was added to each well at the indicated time points following the manufacturer's instructions, and incubated for 2 h. The OD value at 450 nm was detected for each well using a microplate reader (Thermo Fisher Scientific).

Cell viability was also determined using the CCK-8 kit. Cells were seeded at a density of  $1 \times 10^4$  cells per well in 96-well plates. After incubating 12 h, the cells were treated with erastin at the indicated concentrations for 24 h. Finally, cell viability was detected according to the manufacturer's instructions. The percentage of cell viability was calculated using the formula: % cell viability = [(absorbance of the experimental well - absorbance of the blank) / (absorbance of the untreated control well - absorbance of the blank)]  $\times$  100. The 50% inhibitory

concentration (IC<sub>50</sub>) was determined from the concentration–response curve.

For EdU assays,  $4 \times 10^4$  cells per well were seeded into 24-well plates and treated with 50  $\mu$ M EdU reagent for 2 h at 37 °C. After fixation and permeabilization, the cells were detected using the Cell-Light EdU Apollo488 Kit (RiboBio, Guangzhou, China) according to the manufacturer's protocol. Images were captured by LSM880 + 225 Airyscan confocal laser scanning microscope (Carl Zeiss). The proliferation rate was determined by measuring the ratio of EdU-positive cells to DAPI-positive cells.

For the colony formation assay, 1000 cells were plated in 6 cm dishes and cultured for 14–16 days, depending on the growth rate. Colonies were fixed with 4% paraformaldehyde, followed by staining with 0.1% crystal violet (Beyotime) for 20 min. Subsequently, the colonies were photographed and counted.

#### Tube formation assay

Cells were plated at a density of 50% confluence into 10 cm dishes. After 48 h of incubation, the medium was replaced with fresh serum-deprived medium, and the cells were cultured for another 24 h. Subsequently, the conditioned medium (CM) was collected, filtered, and concentrated as described previously [23]. For the tube formation assay, 150  $\mu$ l of Matrigel (Corning, NY, USA) was added to each well of 48-well plates and incubated at 37 °C for 30 min, followed by added HUVECs ( $4 \times 10^4$ ) in 200  $\mu$ l of prepared CM to each well and incubated at 37 °C in 5% CO<sub>2</sub>. After 12 h, bright-field images were captured using an inverted microscope and analyzed with WimTube (<https://www.wimasis.com/en/WimTube>).

#### Chicken chorioallantoic membrane (CAM) assay

The CAM assay was performed using day-7 fertilized chicken eggs (Jinan SAIS Poultry Company, Shandong, China) as described previously [26]. Briefly, sterile gelatin sponges mixed with 20  $\mu$ l of cell suspension containing  $4 \times 10^6$  cells were deposited on the CAM through a window about 1.0 cm in diameter opened in the eggshell. On embryonic developmental days 12 to 14, the CAMs were harvested, fixated, and photographed. The number of new blood vessels was counted.

#### Cytokine arrays and Enzyme-linked immunosorbent assay (ELISA)

Cytokines in the cell supernatant were determined using the G-Series Mouse Inflammation Antibody Array 1 Kit (RayBiotech, GA, USA) by Aksomics Corporation (Shanghai, China) according to the manufacturer's instructions. Fluorescence signals were collected using a laser scanner, and the raw intensities were revised by background.

For the measurement of cytokine concentrations (IL-6, MIP-1 $\alpha$ , and MIG) in the cell supernatant,  $1 \times 10^6$  cells were cultured in 6 cm dishes with 2 mL serum-free medium for 24 h. The cell suspension was then centrifuged, and the supernatant was filtered with a 0.2  $\mu$ m filter. Subsequently, the filtered supernatant was subjected to analyze IL-6, MIP-1 $\alpha$ , and MIG levels using the corresponding mouse ELISA Kits (Thermo Fisher Scientific) according to the manufacturer's instructions.

### RNA-sequencing

The total RNA from sgERO1 $\alpha$  NTC/T1 null and control cells were isolated using TRIzol Reagent (Invitrogen). Gene expression profiles were analyzed through next-generation sequencing (NGS) with Illumina Nova-Seq by Shanghai Biotechnology Corporation (Shanghai China). mRNAs showing a fold change of 2.0-fold or more ( $P < 0.05$ ) were considered differentially expressed. The list of differentially expressed genes was provided as Supplementary Table S8. Kyoto Encyclopedia of Genes and Genomes (KEGG) pathway enrichment analysis was conducted using Xiantao online tools (<https://www.xiantaozi.com/>). The KEGG analysis results were visualized using the Lianchuan Cloud platform (<https://www.omicsstudio.cn/tool/11>). The original data are available at NCBI Gene Expression Omnibus (GEO) under accession number GSE246899.

### In-vivo tumor models

BALB/c-nude mice and NOD/SCID mice were obtained from GemPharmatech. Animal experiments were performed according to the guidelines of the Animal Center of Anhui Medical University, and all detailed experimental procedures were approved by the Experimental Animal Ethical Committee of Anhui Medical University.

For cell line-derived xenograft (CDX) assays, 6-week-old male BALB/c-nude mice were randomly assigned into groups (5 mice per group) to receive respective treatments. To observe the in vivo effect of ERO1 $\alpha$  and SLC7A11,  $4 \times 10^6$  corresponding cell lines in 0.2 ml PBS were subcutaneously inoculated into the axilla of mice to establish tumor models. On day 9 after inoculation with shERO1 $\alpha$ <sup>1</sup> LIU-LSC-1 cells, the mice were treated with Lip-1 (10 mg/kg, once every other day, a total of 10 injections) to assess the impact of ferroptosis inhibition on the tumoral growth of ERO1 $\alpha$ -knockdown cells. To evaluate the therapeutic efficacy of IKE in CDX models, the mice were treated with IKE (30 mg/kg, once every other day) or vehicle for a total of 10 injections on day 17 after inoculation with sgERO1 $\alpha$  NTC/T1 null cells and the control cells.

The LSCC PDX models were established following protocols as described previously [25]. When the passage 3

xenografts reached a mean volume of 100 mm<sup>3</sup>, the mice were randomly divided into 4 groups ( $n = 5$  per group), and treated with ERO1 $\alpha$  siRNA (100  $\mu$ g, three times per week) or siNC, together with IKE (40 mg/kg, once every other day) or vehicle.

Lip-1 and IKE were dissolved in vehicle (10% DMSO, 40% PEG300, 5% Tween 80, and 45% saline) and intraperitoneal injection. The chemically modified ERO1 $\alpha$  siRNAs (GenePharma) were intratumorally injected. Tumor size was measured every 3 days with a digital caliper, and volume was calculated using the standard formula: volume (mm<sup>3</sup>) =  $0.5 \times (\text{length} \times \text{width}^2)$ . Body weights were also monitored. At the endpoint indicated in the corresponding figures, animals were sacrificed, and the subcutaneous tumor masses were taken out for subsequent studies.

### Patient-derived organoid (PDO) model

LSCC organoids were established as described previously with minor modifications [28]. Fresh tumor tissues were washed in ice-cold PBS for  $3 \times 5$  min, and then cut into 1–3 mm<sup>3</sup> fragments on ice. These fragments were subsequently digested with Trypsin (Sigma-Aldrich) for 30 min at 37 °C. The suspension was collected, filtered through a 100  $\mu$ m cell filter, and centrifuged at  $200 \times g$  for 5 min. The obtained cell clusters were embedded in Matrigel (Corning), and then inoculated into pre-warmed 12-well flat-bottom cell culture plate. After polymerization of the Matrigel balls, 1 ml of HNSCC organoid medium (BioGenous, Suzhou, China) was added, and the medium was renewed approximately every 3–5 days.

For lentiviral infection, the organoids were divided into groups of cells using a pipette. Following centrifugation at  $200 \times g$  for 5 min at 4 °C, the cell clusters were suspended in media containing either control lentivirus particles or ERO1 $\alpha$ -knockdown lentivirus particles. Subsequently, they were spin-infected in a centrifuge tube ( $700 \times g$ , 90 min, 25 °C) and incubated at 37 °C for 4 h. Finally, the mixture was centrifuged at  $200 \times g$  for 5 min, and the cell clusters were embedded in Matrigel.

For drug test, the indicated LSCC organoids were inoculated into a 96-well cell culture plate at an appropriate density and covered with 100  $\mu$ L of culture medium. After overnight incubation, the culture medium was replaced with medium containing 50  $\mu$ M IKE. Twenty-four hours later, the cell viability of the organoids was assessed using the Cell Titer-Glo-3D cell viability assay (Promega) following the manufacture's instruction.

### Immunohistochemistry (IHC) analysis

The tumor tissues and organoids were fixed in formalin solution, embedded in paraffin, and sliced into thin sections. After dewaxing, rehydrated, and antigen retrieval,

the sections were incubated with 3% hydrogen peroxide for 1 h to block endogenous peroxidase activity. Next, after pre-incubation with 3% bovine serum albumin for 1 h, the sections were incubated with primary antibodies at 4 °C overnight. The next day, the samples were washed, incubated with HRP-conjugated secondary antibodies, and then developed using DAB solution (Beyotime). Nuclear counterstaining was performed with hematoxylin. A modified histologic score (H-scores [25],  $[\{\% \text{ of weak staining}\} \times 1] + [\{\% \text{ of moderate staining}\} \times 2] + [\{\% \text{ of strong staining}\} \times 3]$ ) was used for quantitative analysis of IHC staining (Supplementary Fig. 10).

### Bioinformatics analysis

Transcriptome datasets of four types of mTORC1-activated cells and their corresponding control cells were obtained from public channels, including *Tsc2*<sup>-/-</sup> vs. *Tsc2*<sup>+/+</sup> MEFs ([https://www.jbc.org/article/S0021-9258\(20\)44588-0/fulltext#supplementaryMaterial](https://www.jbc.org/article/S0021-9258(20)44588-0/fulltext#supplementaryMaterial)), *Tsc1*<sup>-/-</sup> vs. *Tsc1*<sup>+/+</sup> MEFs (SRP056624), ELT3 (*Tsc2*-null rat uterine leiomyoma cells) treated with DMSO vs. ELT3 cells treated with rapamycin (GSE183110), and hiPSCs (human induced pluripotent stem cells) *Tsc2*<sup>-/-</sup> vs. hiPSCs *Tsc2*<sup>+/+</sup> cells (GSE171474). The criteria for screening differentially upregulated genes were  $\log_2 \text{FC} \geq 1$  (or fold change  $\geq 2$ ) and  $P < 0.05$ . The gene lists for all four groups were provided as Supplementary Table S9. We used the online software Venn diagram (<https://bioinformatics.csic.es/tools/venny/>) to identify overlapping genes in the four datasets.

### Statistical analysis

Group differences were analyzed using two-tailed student's t-test or One-way ANOVA as appropriate with GraphPad Prism 6.0 software. A  $p$ -value  $< 0.05$  was considered significant. \* $P < 0.05$ ; \*\* $P < 0.01$ ; \*\*\* $P < 0.001$ ; \*\*\*\* $P < 0.0001$ . All data are expressed as the mean  $\pm$  SD.  $P < 0.05$  was defined as statistically significant.

## Results

### Hyperactivated mTORC1 upregulates ERO1 $\alpha$

Because the TSC1/TSC2 complex is the principal suppressor of mTORC1, *Tsc1* or *Tsc2*-null cells are good models for studying mTORC1 signaling. To identify the functional genes associated with mTORC1 activation across species, we created a Venn diagram using differentially upregulated genes from four transcriptome profiling datasets, including *Tsc2*<sup>-/-</sup> vs. *Tsc2*<sup>+/+</sup> MEFs, *Tsc1*<sup>-/-</sup> vs. *Tsc1*<sup>+/+</sup> MEFs, ELT3 treated with DMSO vs. ELT3 cells treated with rapamycin, and hiPSCs *Tsc2*<sup>-/-</sup> vs. hiPSCs *Tsc2*<sup>+/+</sup> cells [29–32]. Four overlapping upregulated genes were screened, including enolase 3 (*ENO3*), *ERO1 $\alpha$* , hexokinase (*HK2*), and *SLC7A11*

(Fig. 1A). We have previously reported that mTORC1 suppresses melanin synthesis and promotes tumorigenesis through *SLC7A11* upregulation [33]. *HK2* and *ENO3* are representative glycolytic enzymes, and it is well recognized that mTORC1 signaling promotes glycolysis [34–36], whereas the function of *ERO1 $\alpha$*  in mTORC1-activated cells remains unclear. Subsequently, western blot and qRT-PCR analyses confirmed that *ERO1 $\alpha$*  expression was significantly increased in *Tsc1*- or *Tsc2*-null MEFs compared to control cells, and its level was reversed by mTORC1 inhibition with rapamycin treatment (Fig. 1B, C), which was further verified by IF staining (Fig. 1D).

To further substantiate that it is indeed mTORC1 that mediates the positive regulation of *ERO1 $\alpha$*  downstream of the TSC1/TSC2 complex, we detected *ERO1 $\alpha$*  levels in mTOR, Raptor (a specific component of mTORC1) or Rictor (a specific component of mTORC2) knock-down *Tsc2*<sup>-/-</sup> MEFs. As shown in Fig. 1E and Supplementary Fig. 1A, cells transfected with mTOR or Raptor siRNAs exhibited significantly decreased *ERO1 $\alpha$*  levels, while transfection with Rictor siRNAs had little effect on *ERO1 $\alpha$*  expression. A similar result was obtained in *Tsc1*<sup>-/-</sup> MEFs after either knockdown of mTOR, Raptor or Rictor (Fig. 1F, Supplementary Fig. 1B). In contrast, activation of mTORC1 upon treatment of MHY1485 led to upregulation of *ERO1 $\alpha$*  in *Tsc2*<sup>+/+</sup> or *Tsc1*<sup>+/+</sup> MEFs (Fig. 1G). In addition, consistent with the expression of p-S6 (an indicator of mTORC1 activity), the expression of *ERO1 $\alpha$*  was elevated in the renal cystadenomas of *Tsc2*<sup>+/-</sup> mice (Fig. 1H, I). Together, these data suggest that hyperactivated mTORC1 upregulates *ERO1 $\alpha$*  expression.

*ERO1 $\alpha$*  is a hypoxia-responsive gene, and HIF-1 $\alpha$  is a well-known target of mTORC1 [37, 38]. Hence, HIF-1 $\alpha$  may be a candidate transcription factor involved in mTORC1-mediated upregulation of *ERO1 $\alpha$* . As expected, the knockdown of HIF-1 $\alpha$  led to marked downregulation of *ERO1 $\alpha$*  in *Tsc2*<sup>-/-</sup> or *Tsc1*<sup>-/-</sup> MEFs (Supplementary Fig. 2A, B). Moreover, silencing of HIF-1 $\alpha$  suppressed hypoxia-induced (DFX) *ERO1 $\alpha$*  upregulation in *Tsc2*<sup>+/+</sup> or *Tsc1*<sup>+/+</sup> MEFs (Supplementary Fig. 2C, D). Overall, mTORC1 promotes *ERO1 $\alpha$*  expression through HIF-1 $\alpha$  upregulation.

### ERO1 $\alpha$ promotes cell proliferation, angiogenesis, and tumor growth

To clarify the biological functions of *ERO1 $\alpha$*  in mTORC1-activated cells, we silenced *ERO1 $\alpha$*  in *Tsc2*-deficient MEFs using two short hairpin RNAs (shRNAs), designated here as sh*ERO1 $\alpha$* <sup>1</sup> and sh*ERO1 $\alpha$* <sup>2</sup>. Both these *ERO1 $\alpha$* -specific shRNAs efficiently suppressed *ERO1 $\alpha$*  expression compared to the scrambled control shRNA

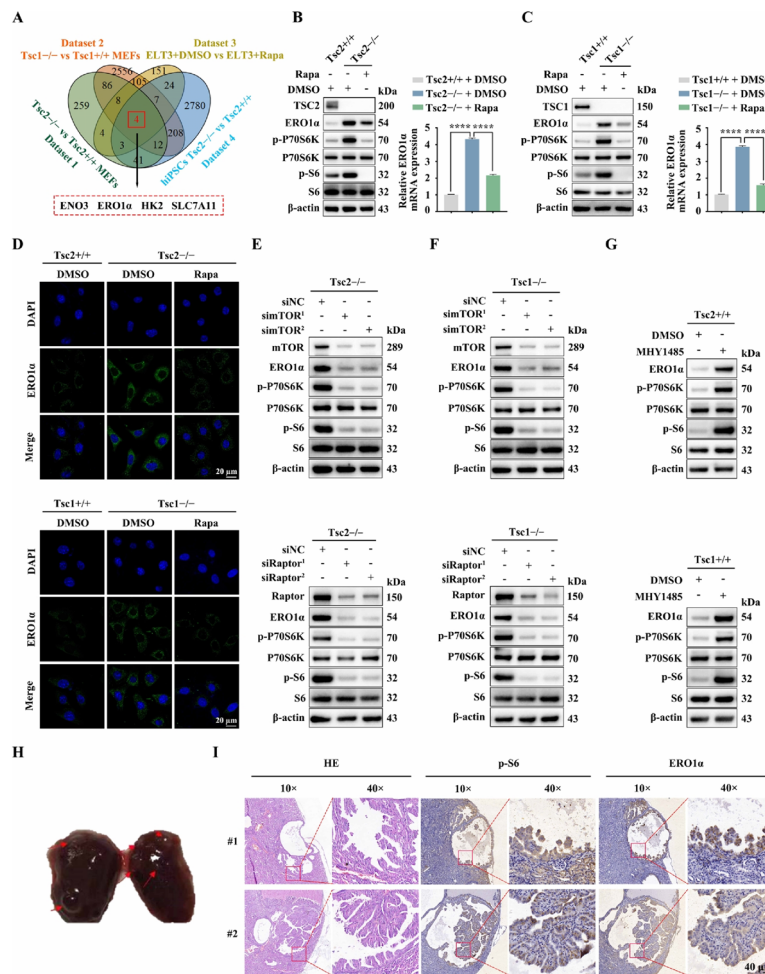


**Fig. 1** mTORC1 upregulates the expression of ERO1 $\alpha$ . **A** Venn diagram analysis of differentially upregulated genes in four datasets. Dataset 1: Tsc2 $^{-/-}$ -vs. Tsc2 $^{+/+}$  MEFs. Dataset 2: Tsc1 $^{-/-}$ -vs. Tsc1 $^{+/+}$  MEFs. Dataset 3: ELT3 cells treated with DMSO vs. ELT3 cells treated with rapamycin (20 nM, 24 h). Dataset 4: hiPSCs Tsc2 $^{-/-}$ -vs. hiPSCs Tsc2 $^{+/+}$ . **B** Tsc2 $^{+/+}$  and Tsc2 $^{-/-}$  MEFs were treated with rapamycin (Rapa, 20 nM) or DMSO for 24 h. **C** Tsc1 $^{+/+}$  and Tsc1 $^{-/-}$  MEFs were treated with rapamycin (Rapa, 20 nM) or DMSO for 24 h. **B** and **C** Cell lysates were subjected to immunoblotting with the indicated antibodies (left panels); ERO1 $\alpha$  levels were analyzed by qRT-PCR (right panels). **D** IF analysis of the expression of ERO1 $\alpha$  in the indicated cells. Scale bar, 20  $\mu$ m. **E** and **F** Tsc2 $^{-/-}$  (E) or Tsc1 $^{-/-}$  (F) MEFs were transfected with siRNA targeting mTOR (simTOR), Raptor (siRaptor) or the control (siNC) for 48 h. **G** Tsc2 $^{+/+}$  or Tsc1 $^{+/+}$  MEFs were treated with 5  $\mu$ M MHY1485 for 24 h. **E-G** Cell lysates were subjected to immunoblotting with the indicated antibodies. **H** A representative kidney of Tsc2 $^{+/+}$  mice. Red arrows indicate renal cysts and cystadenomas. **I** Representative IHC images of p-S6 and ERO1 $\alpha$  staining from renal cystadenomas of Tsc2 $^{+/+}$  mice. Error bars indicate mean  $\pm$  SD of triplicate samples. \*\*\*\* $P$  < 0.0001

(Fig. 2A). CCK-8 and colony formation assays showed that knockdown of ERO1 $\alpha$  significantly reduced the proliferation and colony formation ability of Tsc2 $^{-/-}$  MEFs (Fig. 2B, C). Moreover, an in vitro capillary tube formation assay was used to evaluate the angiogenesis activities of ERO1 $\alpha$ . HUVECs cultured with a conditioned medium derived from ERO1 $\alpha$  knockdown cells developed fewer capillary-like structures and branch points, suggesting the pro-angiogenic effect of ERO1 $\alpha$  (Fig. 2D). This was further proven by a CAM assay, which revealed that knockdown of ERO1 $\alpha$  strongly ablated the formation

of new micro-vessels (Fig. 2E). In addition, ERO1 $\alpha$  was ectopically overexpressed in Tsc2 $^{+/+}$  MEFs (Fig. 2F). In contrast to knockdown of ERO1 $\alpha$ , ERO1 $\alpha$  overexpression promoted cell proliferation, colony formation, and enhanced the angiogenic capacity of Tsc2 $^{+/+}$  MEFs (Fig. 2G-J). In summary, these findings suggest that ERO1 $\alpha$  could promote the proliferation and enhance the pro-angiogenic capacity of mTORC1-activated cells.

Because Tsc1 $^{-/-}$  or Tsc2 $^{-/-}$  MEFs have low tumorigenic ability in vivo [39], we constructed a novel cell line (NTC/T1 null cells) with potent tumorigenicity derived



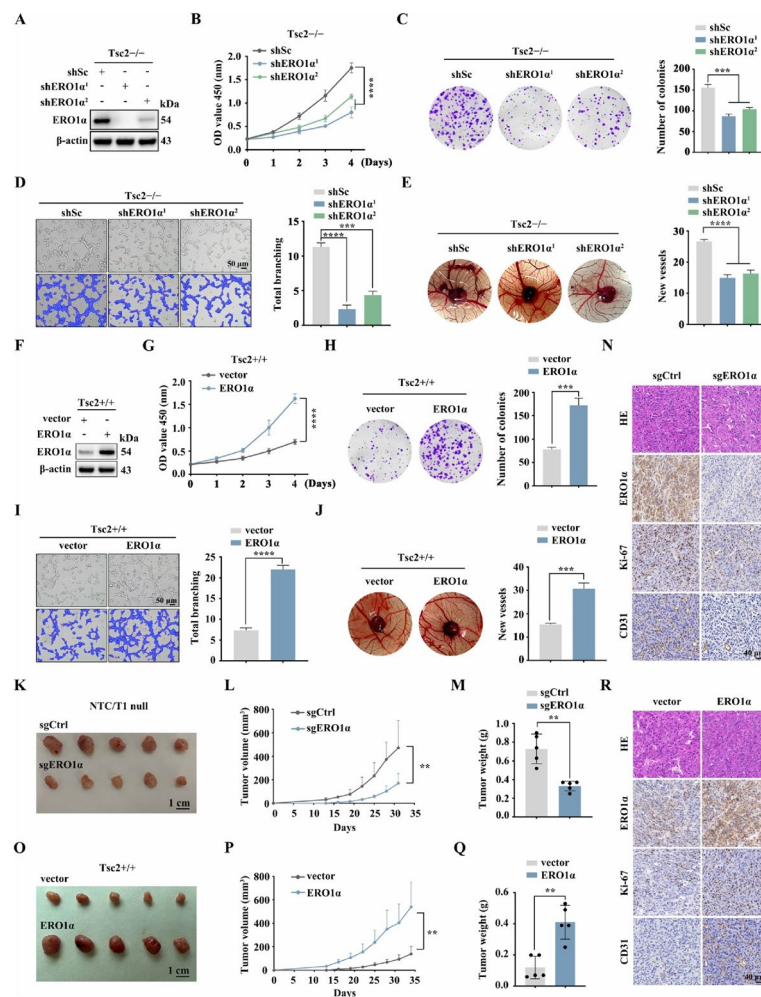


**Fig. 2** ERO1 $\alpha$  promotes cell proliferation, angiogenesis, and tumor growth driven by mTORC1 activation. **A–E** Tsc2 $^{-/-}$  MEFs were transduced with lentivirus expressing shRNAs against ERO1 $\alpha$  (shERO1 $\alpha^1$  and shERO1 $\alpha^2$ ) or a scrambled sequence (shSc). **F–J** Tsc2 $^{+/+}$  MEFs were infected with control (vector) lentiviruses or lentiviruses encoding ERO1 $\alpha$ . **A–J** The expression of ERO1 $\alpha$  was assessed by western blotting (**A** and **F**); the cell proliferation was evaluated by CCK-8 (**B** and **G**) and colony formation (**C** and **H**) assays; the effect on angiogenesis was determined by tube formation (**D** and **I**) and CAM assays (**E** and **J**). Representative images (left panels) and quantifications (right panels). **K–R** Tumor growth of mice subcutaneously inoculated with the indicated cells.  $N=5$  for each group. **K** and **O** Tumor pictures. **L** and **P** Tumor growth curves. **M** and **Q** Tumor weight. **N** and **R** Representative IHC staining for ERO1 $\alpha$ , Ki-67, and CD31 of the indicated tumor tissues. Scale bar, 40  $\mu$ m. Error bars indicate mean  $\pm$  SD of triplicate (if mentioned otherwise) samples. \*\* $P < 0.01$ ; \*\*\* $P < 0.001$ ; \*\*\*\* $P < 0.0001$

from a subcutaneous tumor formed by the injection of Tsc1 $^{-/-}$  MEFs into nude mice to investigate the in vivo role of ERO1 $\alpha$  (Supplementary Fig. 3A–E). ERO1 $\alpha$  was knocked out in NTC/T1 null cells by transfecting with a CRISPR/Cas9 sgRNA lentiviral construct (Supplementary Fig. 3F). As shown in Supplementary Fig. 3G and H, ERO1 $\alpha$  deletion substantially suppressed the proliferative and angiogenic abilities of NTC/T1 null cells. Subsequently, we performed a xenograft assay by subcutaneous injection of sgERO1 $\alpha$  NTC/T1 null cells and control (sgCtrl) cells into the right anterior armpits of nude mice. The mice injected with sgERO1 $\alpha$  cells had significantly

reduced tumor volume and weight compared to those injected with sgCtrl cells (Fig. 2K–M). Furthermore, IHC analysis of mouse xenograft tumor tissues demonstrated a significant reduction in cell proliferative marker Ki-67 and angiogenic marker CD31 levels in sgERO1 $\alpha$  tumors relative to the control counterpart (Fig. 2N). In contrast, the results of a xenograft assay with ERO1 $\alpha$ -overexpressing Tsc2 $^{+/+}$  MEFs showed that overexpression of ERO1 $\alpha$  promotes tumor cell proliferation and angiogenesis in vivo (Fig. 2O–R). Therefore, ERO1 $\alpha$  positively regulates angiogenesis and tumor growth driven by mTORC1 activation.

### Elevated ERO1 $\alpha$ promotes ferroptosis resistance driven by mTORC1 activation

RNA sequencing analysis identified a total 2765 differentially expressed genes (DEGs), including 1376 upregulated genes and 1389 downregulated genes, in sgERO1 $\alpha$  NTC/T1 null cells compared to control cells (Fig. 3A). KEGG pathway analysis for the differentially downregulated genes revealed that the ferroptosis pathway was present among the top 10 dysregulated pathways (Fig. 3B). It has been known that mTORC1 promotes

ferroptosis resistance [13]. Indeed, compared to the control cells, Tsc2- or Tsc1-null MEFs were more resistant to erastin-induced lipid peroxidation and cell death, and this effect could be almost entirely reversed by rapamycin treatment (Supplementary Fig. 4A–E). To verify whether ERO1 $\alpha$  is involved in mTORC1-mediated ferroptosis resistance, we tested sgERO1 $\alpha$  NTC/T1 null cells and the control cells to uncover drug sensitivity with erastin. As shown in the upper panel of Fig. 3C, knockout of ERO1 $\alpha$  increased the sensitivity of NTC/T1 null cells to erastin.

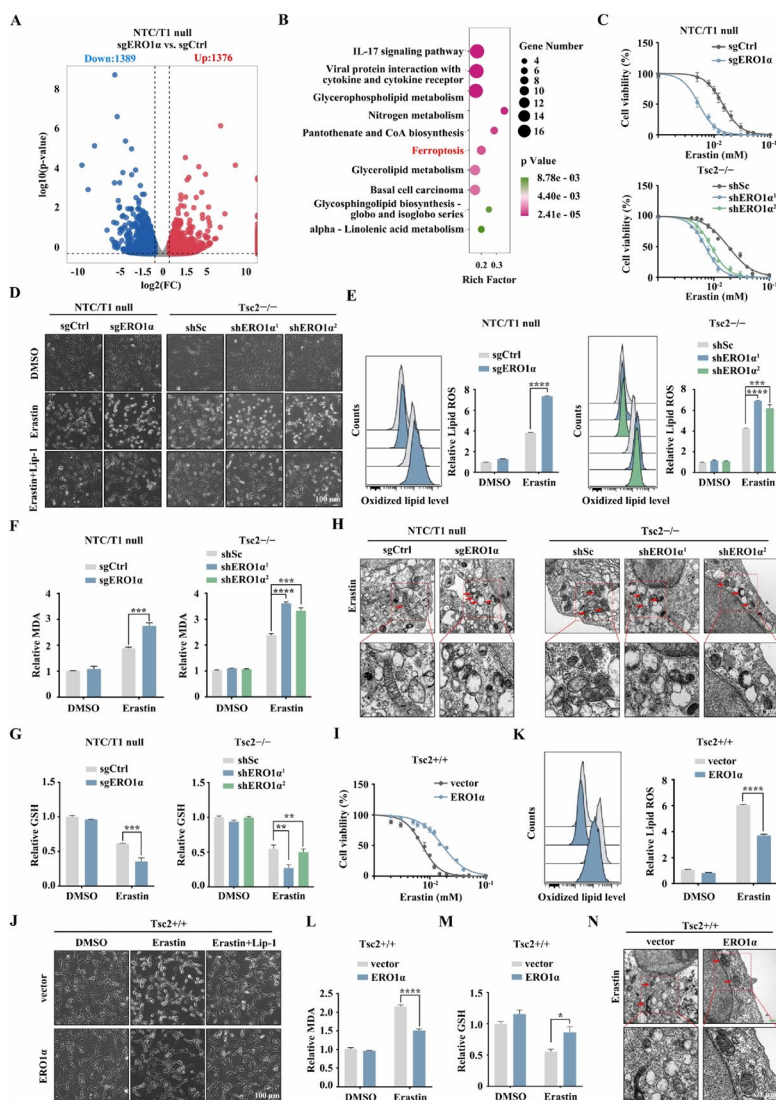


**Fig. 3** ERO1 $\alpha$  facilitates resistance to ferroptosis. **A** and **B** sgERO1 $\alpha$  and sgCtrl NTC/T1 null cells were subjected to RNA-seq analysis. **A** Volcano plot of differentially expressed genes. **B** KEGG enrichment analysis of differentially downregulated genes. **C** and **I** Cell viability of the indicated cells following treatment with erastin for 24 h. **D** and **J** The indicated cells were treated with or without erastin (10  $\mu$ M) in the absence or presence of Lip-1 (1  $\mu$ M) for 24 h. The corresponding phase contrast images are shown. Scale bar, 100  $\mu$ m. **E–G** and **K–M** The indicated cells were treated with or without erastin (10  $\mu$ M) for 24 h, and then L-ROS (**E** and **K**), intracellular MDA (**F** and **L**), and intracellular GSH (**G** and **M**) were assayed. **H** and **N** Representative TEM images of the mitochondrial morphology in the indicated cells treated with 10  $\mu$ M erastin for 16 h. Red arrows indicate mitochondria. Scale bar, 1  $\mu$ m. Error bars indicate mean  $\pm$  SD of triplicate samples. \* $P$  < 0.05; \*\* $P$  < 0.01; \*\*\* $P$  < 0.001; \*\*\*\* $P$  < 0.0001

Similarly, the knockdown of ERO1 $\alpha$  also sensitized erastin to growth inhibition in *Tsc2*<sup>-/-</sup>MEFs (Fig. 3C, lower panel). We also observed that knockout or knockdown of ERO1 $\alpha$  aggravated erastin-induced cell death in NTC/T1 null cells or *Tsc2*<sup>-/-</sup>MEFs (Fig. 3D). Notably, erastin-induced cell death could be rescued by ferroptosis inhibitor Lip-1 (Fig. 3D), which further indicates the occurrence of ferroptosis. We next used BODIPY-C11 (a lipid-soluble ratiometric fluorescent indicator of lipid peroxidation) to estimate the level of ferroptosis-associated lipid peroxidation in ERO1 $\alpha$  knockout or knockdown cells. As represented in Fig. 3E, the depletion of ERO1 $\alpha$  exacerbated erastin-induced lipid peroxidation. Accordingly, ERO1 $\alpha$  silencing also enhanced erastin-induced accumulation of intracellular MDA, which is one of the final products of lipid peroxidation (Fig. 3F). Considering that the loss of cell redox balance causes ferroptosis, GSH plays vital role in eliminating the accumulation of lipid ROS. We next investigated whether ERO1 $\alpha$  depletion is related to GSH synthesis. As shown in Fig. 3G, the GSH levels were significantly suppressed upon ERO1 $\alpha$  knockout or knockdown. Moreover, transmission electron microscopy results showed that ERO1 $\alpha$  knockout or knockdown cells treated with erastin displayed shrunken mitochondria and increased membrane density, a hallmark of ferroptosis. However, these phenotypes were alleviated in control cells after erastin treatment (Fig. 3H). This further indicated that depletion of ERO1 $\alpha$  promoted ferroptosis in mTORC1-activated cells.

To further examine whether ERO1 $\alpha$  induces resistance to ferroptosis, we tested ERO1 $\alpha$ -overexpressing *Tsc2*<sup>+/+</sup>MEFs and the control cells for sensitivity to erastin. As shown in Fig. 3I and J, cells with ectopic expression of ERO1 $\alpha$  were resistant to erastin-induced cell death. Moreover, overexpression of ERO1 $\alpha$  decreased erastin-induced elevation of the peroxide levels and GSH depletion (Fig. 3K–M). Correspondingly, erastin-mediated morphological manifestations related to ferroptosis in mitochondria could be largely reversed by ERO1 $\alpha$  overexpression (Fig. 3N). Our results demonstrate that elevated ERO1 $\alpha$  stimulated ferroptosis resistance in mTORC1-activated cells.

#### **ERO1 $\alpha$ promotes ferroptosis resistance and tumor progression via upregulation of SLC7A11**

Since ERO1 $\alpha$  mediates ferroptosis resistance and tumor growth induced by mTORC1 activation, our next goal is to search for downstream effectors of the mTORC1/ERO1 $\alpha$  pathway. Therefore, a Venn diagram analysis on the ferroptosis-related genes (FRGs) positively regulated by ERO1 $\alpha$  (Fig. 3B) and mTORC1 positively regulated genes (Fig. 1A) was performed. SLC7A11, a critical ferroptosis regulator and tumor promoter, was screened

out (Fig. 4A). Western blot and qRT-PCR analyses confirmed the inhibition of SLC7A11 when ERO1 $\alpha$  knockout was present at both the mRNA and protein levels (Fig. 4B). A consistent result was obtained in *Tsc2*<sup>-/-</sup>MEFs with knockdown of ERO1 $\alpha$  (Supplementary Fig. 5A, B). In contrast, ectopic expression of ERO1 $\alpha$  led to the upregulation of SLC7A11 (Fig. 4C). IF staining confirmed the positive regulatory effect of ERO1 $\alpha$  on SLC7A11 expression (Fig. 4D).

To determine whether the downregulation of SLC7A11 is essential for ERO1 $\alpha$  loss-induced ferroptosis, we re-expressed SLC7A11 in sgERO1 $\alpha$  NTC/T1 null cells by transfecting the *SLC7A11* gene (Fig. 4E). The forced expression of SLC7A11 restored ferroptosis resistance in sgERO1 $\alpha$  cells, which was related to decreased cell death, oxidative damage (L-ROS and MDA), and GSH depletion (Fig. 4F–J). Notably, restoration of SLC7A11 in sgERO1 $\alpha$  cells mostly suppressed erastin-triggered ferroptosis mitochondrial changes, such as shrunken mitochondria and fewer mitochondrial crista (Fig. 4K). Similar to sgERO1 $\alpha$  NTC/T1 null cells, re-expression of SLC7A11 in shERO1 $\alpha$ <sup>1</sup> *Tsc2*<sup>-/-</sup>MEFs inhibited lipid peroxidation and reversed the enhanced sensitivity to erastin upon knockdown of ERO1 $\alpha$  (Supplementary Fig. 5C–H). To further explicate the effect of SLC7A11 in ERO1 $\alpha$ -mediated ferroptosis resistance, we silenced endogenous SLC7A11 by transducing lentiviral vectors expressing shRNA for SLC7A11 to ERO1 $\alpha$ -overexpressing *Tsc2*<sup>+/+</sup>MEFs. The knockdown efficiency was confirmed by western blotting (Fig. 4L). As expected, SLC7A11 knockdown reversed the resistance of ERO1 $\alpha$ -overexpressing *Tsc2*<sup>+/+</sup>MEFs to erastin-induced growth inhibition, cell death, lipid peroxidation, GSH downregulation, and changes in mitochondrial morphology (Fig. 4M–R).

Next, we examined whether the pro-oncogenic effect of ERO1 $\alpha$  in mTORC1-activated cells depends on SLC7A11. As shown in Fig. 5A, restoration of SLC7A11 in sgERO1 $\alpha$  cells partially rescued ERO1 $\alpha$  knockout-induced suppression of cell growth. Moreover, the proliferative ability of sgERO1 $\alpha$  cells was significantly promoted by SLC7A11 re-expression, as determined by EdU staining (Fig. 5B, C). Furthermore, tube formation and CAM assays demonstrated that SLC7A11 overexpression attenuated the inhibitory effect of ERO1 $\alpha$  deficiency on angiogenesis (Fig. 5D, E). Consistent with sgERO1 $\alpha$  NTC/T1 null cells, restoration of SLC7A11 efficiently reversed the adverse effects of ERO1 $\alpha$  knockdown on the proliferative and angiogenic abilities of *Tsc2*<sup>-/-</sup>MEFs (Supplementary Fig. 6A–D). In contrast, the accelerated cell proliferation and angiogenesis induced by ERO1 $\alpha$  overexpression were inhibited by knockdown of SLC7A11 in *Tsc2*<sup>+/+</sup>MEFs (Fig. 5F–J). Overall, these data underscore the



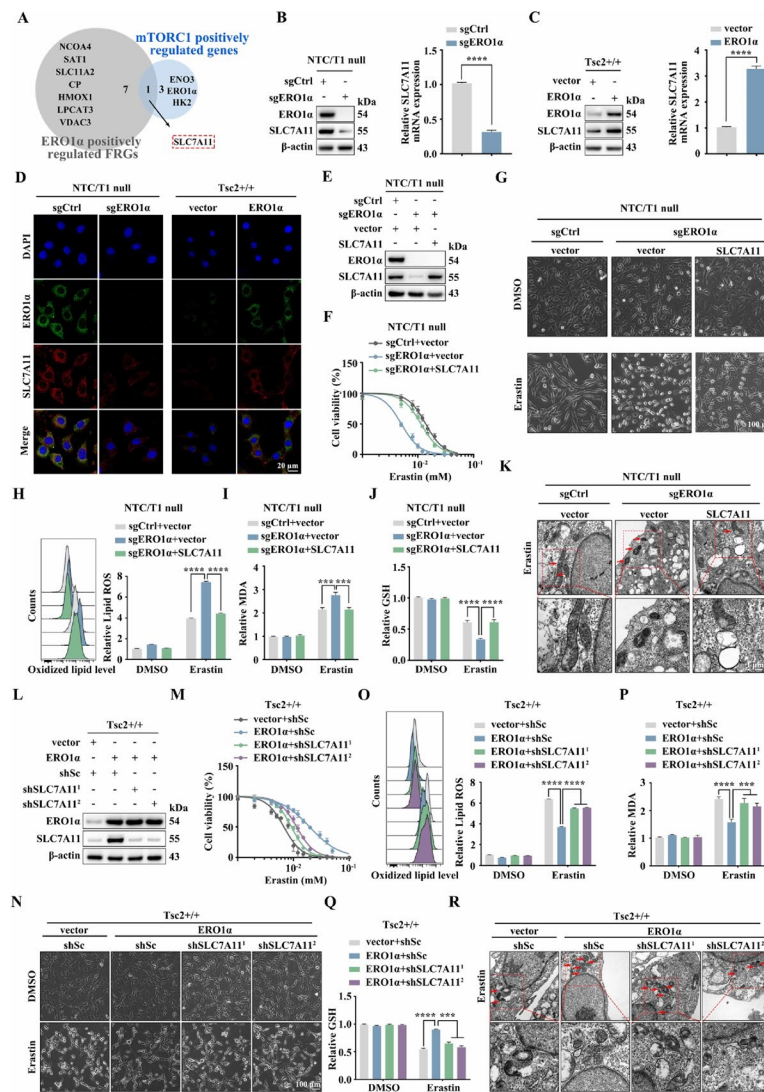


**Fig. 4** ERO1 $\alpha$  facilitates ferroptosis resistance through the upregulation of SLC7A11. **A** Venn diagram of the ferroptosis-related genes (FRGs) positively regulated by ERO1 $\alpha$  and mTORC1 positively regulated genes. **B** sgERO1 $\alpha$  and sgCtrl NTC/T1 null cells. **C** ERO1 $\alpha$ -overexpressing Tsc2 $^{+/+}$  MEFs and the control cells. **B** and **C** SLC7A11 levels were examined by western blotting (left panels) and qRT-PCR (right panels). **D** IF analysis of the expression of SLC7A11 in the indicated cells. Scale bar, 20  $\mu$ m. **E–K** sgERO1 $\alpha$  NTC/T1 null cells were infected with lentiviruses carrying an empty vector (vector) or expression vectors for SLC7A11. **L–R** ERO1 $\alpha$ -expressing Tsc2 $^{+/+}$  MEFs were infected with lentivirus harboring SLC7A11 shRNAs (shSLC7A11 $^1$  and shSLC7A11 $^2$ ) or a scrambled shRNA (shSc). **E** and **L** SLC7A11 and ERO1 $\alpha$  protein levels were examined by western blotting. **F** and **M** Cell viability was assessed after treatment with different concentrations of erastin for 24 h in the indicated cells. **G** and **N** Representative phase-contrast images of the indicated cells treated with erastin (10  $\mu$ M, 24 h) or DMSO. Scale bar, 100  $\mu$ m. **H–J** and **O–Q** The indicated cells were treated with or without erastin (10  $\mu$ M) for 24 h, and then L-ROS (**H** and **O**), intracellular MDA (**I** and **P**), and intracellular GSH (**J** and **Q**) were measured. **K** and **R** Representative TEM images of the indicated cells treated with 10  $\mu$ M erastin for 16 h. Red arrows indicate mitochondria. Scale bar, 1  $\mu$ m. Error bars indicate mean  $\pm$  SD of triplicate samples. \*\*\* $P$  < 0.001; \*\*\*\* $P$  < 0.0001

importance of ERO1 $\alpha$ -regulated SLC7A11 expression in the tumorigenesis of mTORC1-activated cells.

The mediation effect of SLC7A11 on ERO1 $\alpha$ -regulated cell growth and angiogenesis was further verified in vivo using a subcutaneous xenograft tumor model. Consistent with the in vitro results, SLC7A11 re-expression abrogated the suppressive effects of

ERO1 $\alpha$  depletion on xenograft growth, tumor cell proliferation (as assessed by the Ki-67 index), and tumor angiogenesis (as assessed by the CD31 index) (Fig. 5K–O). Conversely, ERO1 $\alpha$  overexpression-induced xenograft tumor development and ferroptosis inhibition were significantly attenuated with suppression of SLC7A11 (Fig. 5P–T). Our results indicate that ERO1 $\alpha$



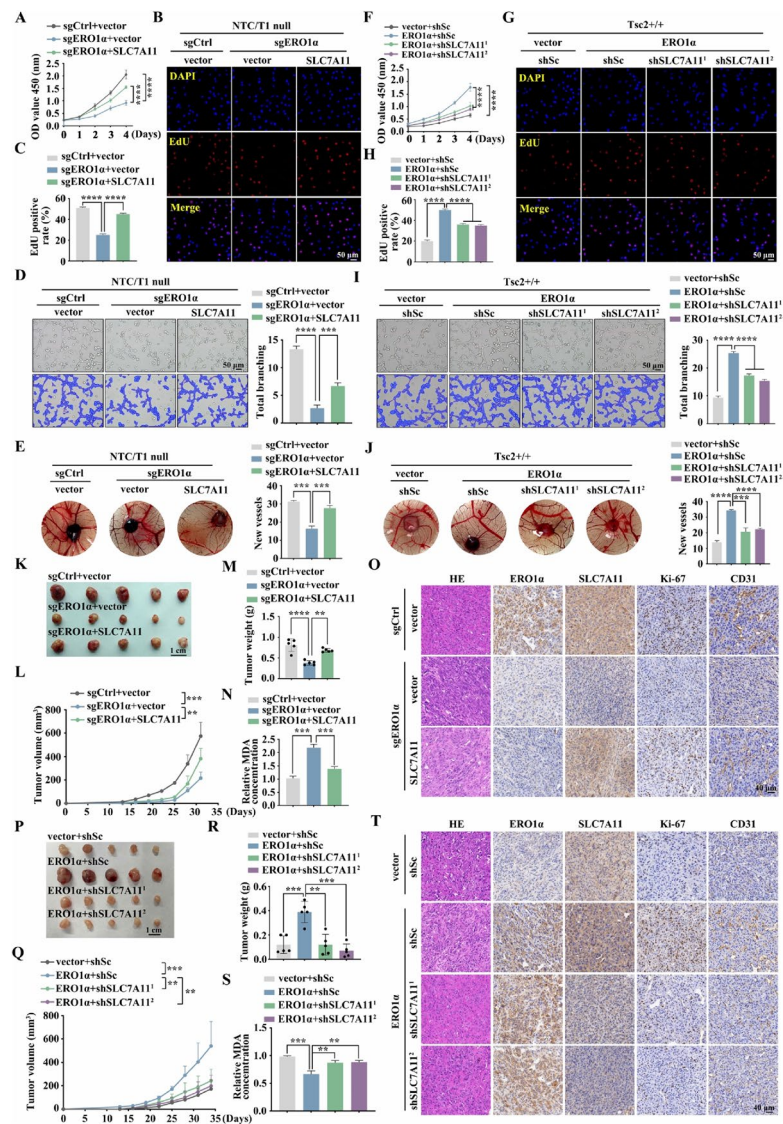


**Fig. 5** ERO1 $\alpha$  exhibits tumor-promoter activities through the upregulation of SLC7A11. **A–E** sgERO1 $\alpha$  NTC/T1 null cells were infected with lentiviruses carrying an empty vector (vector) or expression vectors for SLC7A11. **F–J** ERO1 $\alpha$ -overexpressing Tsc2 $^{+/+}$  MEFs were infected with lentivirus harboring SLC7A11 shRNAs (shSLC7A11<sup>1</sup> and shSLC7A11<sup>2</sup>) or a scrambled shRNA (shSc). CCK-8 (**A** and **F**) and EdU (**B**, **C**, **G** and **H**) assays were performed to evaluate cell proliferation. Scale bar, 50  $\mu$ m. The effect on angiogenesis was determined by tube formation (**D** and **I**) and CAM (**E** and **J**) assays. Representative images (left panels) and quantifications (right panels). Scale bar, 50  $\mu$ m. **K–T** sgERO1 $\alpha$  NTC/T1 null cells, with or without SLC7A11 re-expression (**K–O**), and ERO1 $\alpha$ -overexpressing Tsc2 $^{+/+}$  MEFs, with or without SLC7A11 knockdown (**P–T**), were subcutaneously injected into nude mice for xenograft assays. **K** and **P** Pictures of the removed tumors. **L** and **Q** The size of xenograft tumors was measured. **M** and **R** Tumors were weighed and plotted. **N** and **S** The relative MDA levels of the indicated tumors were measured. **O** and **T** Representative IHC images for ERO1 $\alpha$ , SLC7A11, Ki-67, and CD31 proteins of the indicated xenograft tumors. Scale bar, 40  $\mu$ m. Error bars indicate mean  $\pm$  SD of triplicate (if mentioned otherwise) samples. \*\* $P$  < 0.01; \*\*\* $P$  < 0.001; \*\*\*\* $P$  < 0.0001

promotes tumor progression and ferroptosis resistance, at least partially, by upregulating SLC7A11.

#### ERO1 $\alpha$ upregulates SLC7A11 via activation of the IL-6/STAT3 pathway

As a key enzyme for disulfide bond formation, ERO1 $\alpha$  plays a critical role in the folding process of the new

peptide chain to form a functional secreted protein [40, 41]. Therefore, we next collected the conditioned media from sgERO1 $\alpha$  NTC/T1 null cells, shERO1 $\alpha$ <sup>1</sup> Tsc2 $^{-/-}$  MEFs, and their corresponding control cells and conducted a cytokine array assay (Fig. 6A). Results showed that three cytokines, including IL-6, MIP-1 $\alpha$ , and MIG, were significantly decreased upon knockout

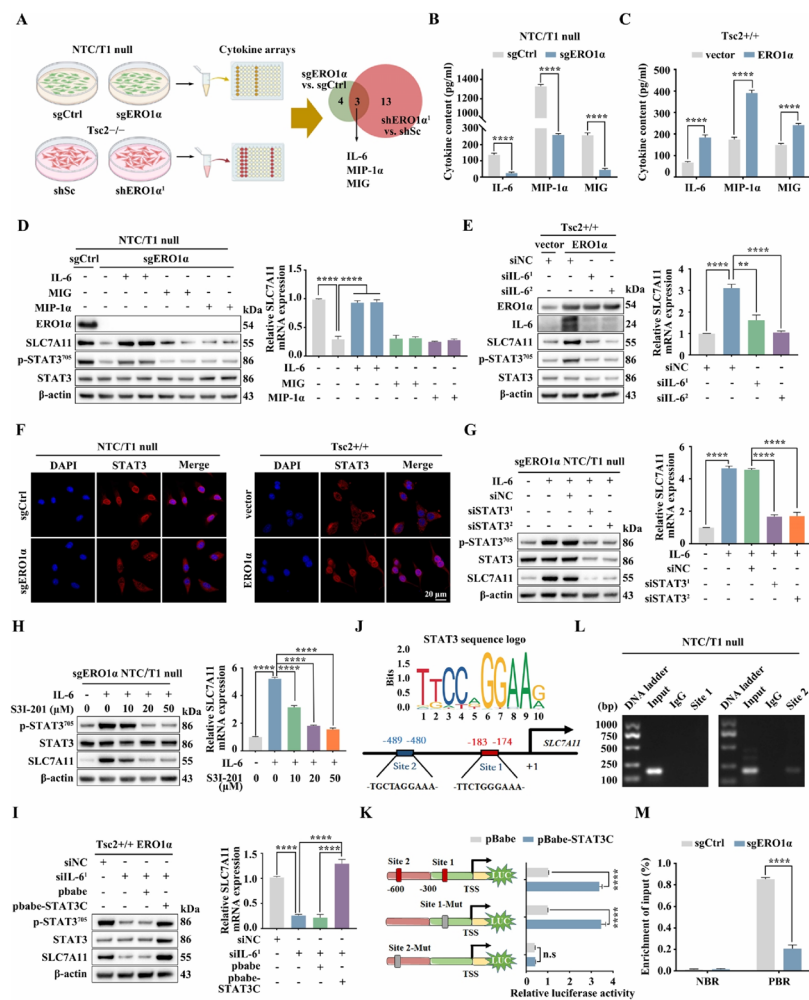


**Fig. 6** ERO1α upregulates SLC7A11 via activation of the IL-6/STAT3 pathway. **A** Schematic diagram of the screening of co-differentially expressed cytokines upon knockout or knockdown of ERO1α using a cytokines array assay. **B** and **C** Cell supernatants from the indicated cells were collected, and IL-6, MIP-1α, and MIG levels were determined using an ELISA. **D** sgERO1α NTC/T1 null cells were treated with IL-6 (20 ng/ml), MIP-1α (100 ng/ml), or MIG (100 ng/ml) for 24 h. **E** ERO1α-overexpressing Tsc2+/+ MEFs were transfected with IL-6 siRNAs or control siRNA (siNC) for 48 h. **D** and **E** Cell lysates were subjected to immunoblotting with the indicated antibodies (left panels), the expression of SLC7A11 mRNA was detected by qRT-PCR (right panels). **F** Representative IF showing the localizations of STAT3 in the indicated cells. Scale bar, 20 μm. **G** IL-6 (20 ng/ml, 12 h) pre-treated sgERO1α NTC/T1 null cells were transfected with STAT3 siRNAs or control siRNA (siNC) for 48 h. **H** IL-6 (20 ng/ml, 12 h) pre-treated sgERO1α NTC/T1 null cells were treated with different concentrations of S31-201 for 24 h. **I** IL-6 siRNA-transduced ERO1α-overexpressing Tsc2+/+ MEFs were transfected with a constitutively activated STAT3 (STAT3C) or its control vector pBabe-puro (pBabe). **G–I** The expression of SLC7A11 was examined by western blotting (left panels) and qRT-PCR (right panels). **J** Schematic representation of the putative STAT3-binding sites in the promoter of mouse *SLC7A11* gene. **K** HEK 293 T cells were co-transfected with the indicated promoter constructs plus pBabe-STAT3C or empty vector pBabe and the internal control plasmid pRL-TK. The relative luciferase activity was determined 24 h after transfection. **L** The enrichment of STAT3 in the promoter of *SLC7A11* was analyzed by ChIP-PCR assay. **M** sgERO1α and sgCtrl NTC/T1 null cells were subjected to ChIP analysis with antibodies to p-STAT3 or control rabbit IgG. qRT-PCR was performed to amplify regions surrounding the putative STAT3 binding Site 2 (PBR) and a nonspecific STAT3 binding region (NBR). The data were plotted as the ratio of immunoprecipitated DNA to total input DNA. Error bars indicate mean ± SD of triplicate samples. \*\**P* < 0.01; \*\*\*\**P* < 0.0001. n.s.: no significance

and knockdown of ERO1α in mTORC1-activated cells (Supplementary Fig. 7A). ELISA assays confirmed that ERO1α depletion markedly downregulated the levels of secreted IL-6, MIP-1α, and MIG in NTC/T1 null cells and Tsc2−/− MEFs. However, overexpression of ERO1α promoted the expression of these cytokines (Fig. 6B,

C, Supplementary Fig. 7B). IL-6 treatment rescued the decreased levels of SLC7A11 induced by knockout or knockdown of ERO1α. In contrast, administration of MIP-1α and MIG had little effect on the expression of SLC7A11 in ERO1α knockout or knockdown cells (Fig. 6D, Supplementary Fig. 7C). Therefore, ERO1α

likely promotes the expression of SLC7A11 by upregulating of IL-6. In line with this view, the knockdown of IL-6 abrogated the overexpression of ERO1 $\alpha$ -induced upregulation of SLC7A11 in Tsc2 $+/+$ MEFs (Fig. 6E). It is well known that IL-6 drives oncogenic activation of STAT3 in multiple cells [42]. Interestingly, IL-6 treatment reversed the attenuated STAT3 activity driven by depletion of ERO1 $\alpha$  in NTC/T1 null or Tsc2 $-/-$ MEFs, while knockdown of IL-6 attenuated the enhanced STAT3 activity due to ERO1 $\alpha$  overexpression in Tsc2 $+/+$ MEFs (Fig. 6D, E, Supplementary Fig. 7C). IF analysis also confirmed that the nuclear accumulation of STAT3 was positively regulated by ERO1 $\alpha$  (Fig. 6F, Supplementary Fig. 7D). Moreover, inhibition of STAT3 by genetic or pharmacologic strategies suppressed IL-6-induced upregulation of SLC7A11 in sgERO1 $\alpha$  NTC/T1 null cells (Fig. 6G, H). A similar result was also observed in ERO1 $\alpha$ -KD Tsc2 $-/-$ MEFs (Supplementary Fig. 7E, F). On the contrary, overexpression of the constitutively activated form of STAT3 (STAT3C) significantly compromised the inhibitory effect of IL-6 knockdown on SLC7A11 expression in ERO1 $\alpha$ -overexpressing Tsc2 $+/+$ MEFs (Fig. 6I). Hence, we propose that ERO1 $\alpha$  stimulates SLC7A11 expression via activation of the IL-6/STAT3 pathway.

To further investigate the mechanisms underlying STAT3 regulation of SLC7A11, we analyzed the potential upstream promoter region ( $-2000$  to  $+200$ ) of mouse SLC7A11 using JASPAR (<http://jaspar.genereg.net>), which predicted two possible binding regions of STAT3 (Fig. 6J). We then cloned the mouse SLC7A11 gene promoter ( $-575$  to  $+144$ ) into the pGL3 luciferase reporter vector and evaluated the effect of STAT3 on the promoter activity. The promoter activity of the wild-type SLC7A11 construct was enhanced by STAT3C overexpression. Notably, mutation of Site 2 completely abolished the stimulatory effect of STAT3C, whereas mutation of Site 1 showed only a slight effect on STAT3C-induced SLC7A11 promoter activity (Fig. 6K). The ChIP-PCR

assay indicated that STAT3 was only enriched at Site 2, further suggesting that this site is critically important for the transcription of SLC7A11 (Fig. 6L). Moreover, the ChIP-qRT-PCR assay revealed decreased occupancy of STAT3 on the SLC7A11 promoter in sgERO1 $\alpha$  cells and increased occupancy in ERO1 $\alpha$ -overexpressing cells (Fig. 6M, Supplementary Fig. 7G). Therefore, we conclude that activated STAT3 transcriptionally elevates SLC7A11 by directly binding to its promoter in response to the ERO1 $\alpha$ /IL-6 pathway activation.

### The mTORC1/ERO1 $\alpha$ /IL-6/STAT3/SLC7A11 signaling pathway presents in human cancer

mTORC1 signaling is aberrantly activated in many cancers, including LSCC [25]. To examine whether the newly discovered mTORC1 regulation of the ERO1 $\alpha$ /SLC7A11 pathway is also detectable in human cancer cells, a mTORC1-hyperactivated LSCC cell line, LIU-LSC-1, was employed [25]. As shown in Fig. 7A and B, the knockdown of Raptor led to the downregulation of ERO1 $\alpha$ , IL-6, p-STAT3, and SLC7A11 in LIU-LSC-1 cells. Inhibition of mTORC1 with rapamycin achieved a similar result (Supplementary Fig. 8A). Moreover, manipulation of the activity of mTORC1 by TSC2 knockout increased the expressions of ERO1 $\alpha$ , IL-6, p-STAT3, and SLC7A11 in TU177 cells (an LSCC cell line with moderate mTORC1 activity) (Supplementary Fig. 8B). In addition, genetic or pharmacological inhibition of mTORC1 led to a similar result in other types of mTORC1-activated cancer cells, such as PANC-1, MDA-MB-231, A549 and HeLa (Supplementary Fig. 8C, D). Because mTORC1 regulates the ERO1 $\alpha$ /SLC7A11 signaling network in multiple human cancer cell lines in vitro, we predicted that this signaling regulation should also exist in human tumors in vivo. As depicted in Fig. 7C and D and Supplementary Fig. 8E, ERO1 $\alpha$ , IL-6, p-STAT3, and SLC7A11 levels were substantially elevated in most of the 24 LSCC tissues tested, and p-S6 levels were significantly enhanced

(See figure on next page.)

**Fig. 7** The mTORC1/ERO1 $\alpha$ /IL-6/STAT3/SLC7A11 signaling pathway exists in human cancer. **A** and **B** LIU-LSC-1 cells were infected with lentivirus expressing shRNAs targeting Raptor (shRaptor<sup>1</sup> and shRaptor<sup>2</sup>) or a control shRNA (shSc). Cell lysates were subjected to immunoblotting with the indicated antibodies (**A**), ERO1 $\alpha$  and SLC7A11 mRNA levels were detected by qRT-PCR (**B**). **C** 12 paired LSCC tissues and the corresponding ANM tissues were subjected to immunoblotting with the indicated antibodies. **D** Representative IHC images of p-S6, ERO1 $\alpha$ , IL-6, p-STAT3, and SLC7A11 staining from the LSCC tissues and ANM tissues. Scale bar, 20  $\mu$ m. **E-I** LIU-LSC-1 were infected with lentiviruses expressing shRNAs targeting ERO1 $\alpha$  (shERO1 $\alpha$ <sup>1</sup> and shERO1 $\alpha$ <sup>2</sup>) or a non-targeting shRNA (shSc). **E** The protein and mRNA levels of ERO1 $\alpha$  and SLC7A11 were determined by western blotting and qRT-PCR. **F** and **G** CCK-8 (**F**) and colony formation (**G**) assays were performed to evaluate cell growth. **H** and **I** The pro-angiogenic effect of ERO1 $\alpha$  was detected by tube formation (**H**) and CAM assays (**I**). Representative images (left panels) and quantifications (right panels) are shown. **J** Cell viability of indicated cells following treatment with erastin for 24 h. **K** Representative phase-contrast images of indicated cells were treated with erastin (15  $\mu$ M) in the absence or presence of Lip-1 (1  $\mu$ M). The corresponding phase contrast images are shown. Scale bar, 100  $\mu$ m. **L-N** The indicated cells were treated with or without erastin (15  $\mu$ M) for 24 h, and then intracellular MDA (**L**), L-ROS (**M**), and intracellular GSH (**N**) were measured. **O-R** Tumor images (**O**), tumor volume (**P**), and tumor weight (**Q**) of shERO1 $\alpha$ <sup>1</sup> LIU-LSC-1 xenograft tumors ( $n=5$  mice/group) treated with Lip-1 (10 mg/kg) or vehicle. **R** The relative MDA levels of the indicated tumors were measured. Error bars indicate mean  $\pm$  SD of triplicate (if mentioned otherwise) samples. \*\* $p < 0.01$ ; \*\*\* $p < 0.001$ ; \*\*\*\* $p < 0.0001$



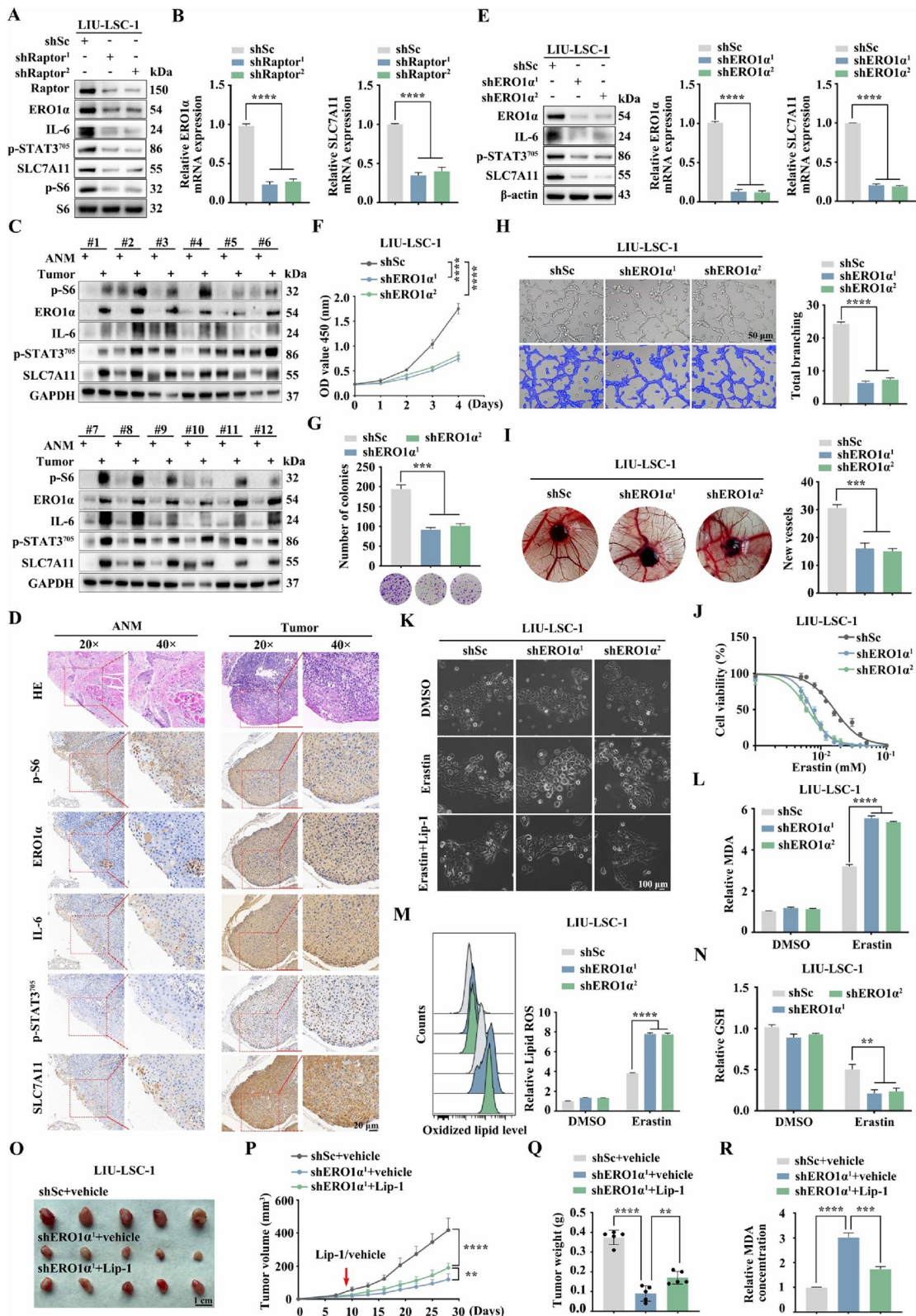


**Fig. 7** (See legend on previous page.)



in these tissues, but not in the corresponding ANM tissues. Therefore, the regulatory pathway of SLC7A11 by the ERO1 $\alpha$ /IL-6/STAT3 axis presents in human cancer cells with hyperactivated mTORC1 signaling.

To confirm the pro-oncogenic and anti-ferroptotic roles of ERO1 $\alpha$  in human cancer cells, two shRNAs, especially targeting ERO1 $\alpha$  were transfected into LIU-LSC-1 cells. The knockdown efficiency was confirmed by western blotting (Fig. 7E). Consistent with MEFs, the depletion of ERO1 $\alpha$  led to downregulated expression of IL-6, p-STAT3, and SLC7A11 in LIU-LSC-1 cells (Fig. 7E). We also confirmed that knockdown of ERO1 $\alpha$  reduced the proliferative and angiogenic capacities of LIU-LSC-1 cells (Fig. 7F–I). Not surprisingly, in line with MEFs, LIU-LSC-1 shERO1 $\alpha$  cells exhibited a greater susceptibility to erastin, which could be rescued by Lip-1 (Fig. 7J, K). Notably, ERO1 $\alpha$  knockdown cells exhibited increased lipid peroxidation (L-ROS and MDA) and GSH depletion (Fig. 7L–N). Additionally, through the subcutaneous injection of LIU-LSC-1 cells in three groups (shSc + vehicle, shERO1 $\alpha$ <sup>1</sup> + vehicle, and shERO1 $\alpha$ <sup>1</sup> + Lip-1) of nude mice, xenograft animal models were obtained to confirm the anti-ferroptosis effects of ERO1 $\alpha$  again. Repression of ERO1 $\alpha$  reduced the sizes of developed tumors and increased MDA levels, which did not occur in the control group. However, Lip-1 partially reverses the growth inhibition and ferroptotic events induced by silencing ERO1 $\alpha$  (Fig. 7O–R). Overall, the mTORC1/ERO1 $\alpha$ /IL-6/STAT3/SLC7A11 signaling cascade, which is also present in human cancer cells, plays a critical role in ferroptosis resistance and tumor progression.

#### Targeting ERO1 $\alpha$ significantly enhances the antitumor effect of IKE

The data above revealed that ERO1 $\alpha$  significantly contributed to tumor progression and ferroptosis resistance, encouraging us to explore whether inhibition of ERO1 $\alpha$  in combination with ferroptosis inducers could synergistically inhibit the growth of mTORC1-activated cells in vivo. sgERO1 $\alpha$  NTC/T1 null cells and control cells were inoculated into nude mice to form subcutaneous tumors. The mice were treated with IKE, a metabolically stable analog of erastin, or vehicle [43] (Supplementary Fig. 9A). Consistent with our in vitro observations, ERO1 $\alpha$  knockout NTC/T1 cells were more sensitive to IKE-induced tumor suppression than control cells in vivo (Supplementary Fig. 9B–D). IHC staining further revealed decreased Ki-67 and increased 4-HNE staining after IKE treatment, and these effects were markedly strengthened by ERO1 $\alpha$  depletion (Supplementary Fig. 9E). Moreover, ERO1 $\alpha$  deficiency resulted in therapy sensitivity, which was associated with increased MDA levels (Supplementary Fig. 9F). Notably, there was no

loss of body weight in the treated mice (Supplementary Fig. 9G).

Considering that PDO and PDX tumor models can highly preserve the heterogeneity and histological characteristics of the original tumors [44], we further tested the therapeutic potential of combining ERO1 $\alpha$  inhibition and IKE in tumor treatment using PDO and PDX models (Fig. 8A). As shown in Fig. 8B, histological analysis confirmed that these LSCC organoids retained the histological features of the original tumors. Similar to our observations in the CDX models, the depletion of ERO1 $\alpha$  significantly aggravated the inhibitory effect of IKE on the growth of LSCC organoids (Fig. 8C, D). Furthermore, fresh LSCC tumors with activated mTORC1 and high levels of ERO1 $\alpha$  were chosen to establish the PDX models (Fig. 8E, F). Because no current ERO1 $\alpha$  inhibitor is suitable for in vivo treatment, we used ERO1 $\alpha$  siRNAs to knock down ERO1 $\alpha$  in our animal studies. We showed that co-treatment with ERO1 $\alpha$  siRNAs and IKE suppressed PDX tumor growth much more potently than either treatment alone (Fig. 8G–I). Successful in vivo knockdown of ERO1 $\alpha$  in tumors by siRNAs was confirmed by IHC analysis (Fig. 8J). Further analyses revealed that the combination treatment, which was well tolerated in vivo, synergistically increased the staining of 4-HNE and the production of MDA in PDX tumor samples (Fig. 8J–L). Our results show that ERO1 $\alpha$  inhibition sensitizes mTORC1-activated cells to ferroptosis. This suggests combining ERO1 $\alpha$  inhibition with ferroptosis inducers in the treatment of mTORC1-related cancer to achieve better outcomes.

#### Discussion

Increasing research indicates that mTORC1, which is aberrantly activated in many types of human cancers, is critical for promoting tumor development [6, 8]. However, its underlying mechanisms still need to be fully understood. Currently, even though rapamycin and its derivatives have been approved for use in the treatment of several mTORC1-associated tumors, such as breast cancer, advanced renal cancer, and tuberous sclerosis complex, their clinical therapeutic effects are minimal [45–47]. One key reason for this is that suppression of mTORC1 leads to feedback activation of AKT [46]. Therefore, it is urgent to identify novel therapeutic targets and develop new approaches for mTORC1-related cancers. In this study, which primarily focused on mTORC1-activated MEFs and cancer cell lines, LSCC tissues, organoids, and PDX models, we identified ERO1 $\alpha$  as a functional downstream target of mTORC1. We also illustrated that elevated ERO1 $\alpha$  expression contributes to tumor progression driven by mTORC1 activation. In addition, we found that mTORC1 promotes the

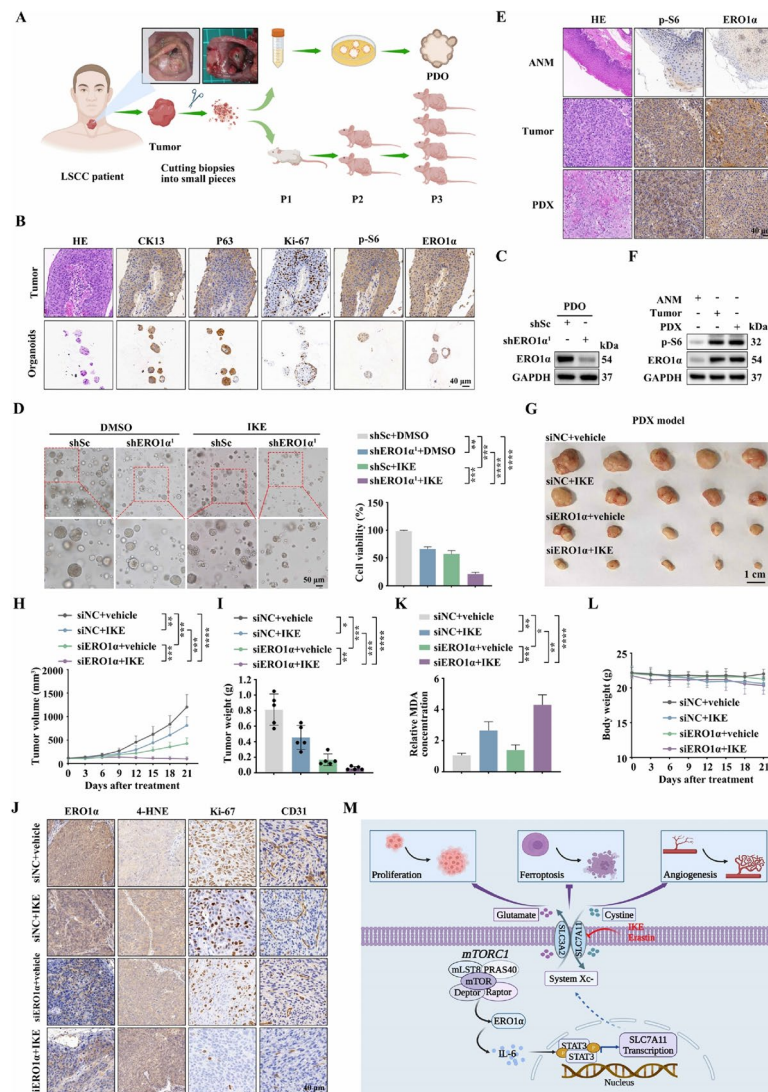


**Fig. 8** The combination of ERO1 $\alpha$  inhibition and IKE exerts an effective inhibitory effect on the growth of PDO and PDX models. **A** Schematic workflow of the generation of LSCC organoids and PDX models. **B** Representative IHC images of CK13, p63, Ki-67, p-S6, and ERO1 $\alpha$  staining from LSCC tissues and organoids. Scale bar, 40  $\mu$ m. **C** LSCC organoids were infected with lentiviruses expressing shRNAs targeting ERO1 $\alpha$  (shERO1 $\alpha$ <sup>1</sup>) or a non-targeting shRNA (shSc). The level of ERO1 $\alpha$  was detected by western blotting. **D** shERO1 $\alpha$ <sup>1</sup> or shSc lentiviruses-infected organoids were treated with IKE (50  $\mu$ M) or DMSO for 24 h. The cell viability of organoids was determined by Cell-Titer Glo-3D cell viability assay. Left panels: representative phase contrast images. Right panels: quantitation of the data. Scale bar, 50  $\mu$ m. **E** and **F** The expression of p-S6 and ERO1 $\alpha$  in the PDX tumor tissues, primary tumor tissues and ANM tissues were analyzed by IHC (**E**) and western blotting (**F**). **G–I** Tumor images (**G**), tumor volume (**H**), and tumor weight (**I**) of PDX model tumors treated with ERO1 $\alpha$  siRNAs or siNC, together with IKE (40 mg/kg) or vehicle. *n* = 5 mice per group. **J** IHC staining of PDX tumor tissues using the indicated antibodies. Scale bar, 40  $\mu$ m. **K** MDA assay was used to detected lipid peroxidation levels in randomly selected PDX tumor section. **L** Body weight of mice. **M** Schematic illustration of the activated ERO1 $\alpha$ /IL-6/STAT3/SLC7A11 pathway is critical for mTORC1-mediated ferroptosis resistance and tumor progression. Error bars indicate mean  $\pm$  SD of triplicate (if mentioned otherwise) samples. \**P* < 0.05; \*\**P* < 0.01; \*\*\**P* < 0.001; \*\*\*\**P* < 0.0001

transcription of ERO1 $\alpha$  by upregulating the transcription factor HIF-1 $\alpha$ , a well-known mTORC1 downstream effector. This agree with previous findings suggesting that ERO1 $\alpha$  is a hypoxia-inducible gene in many cell lines [48]. Recently, the crucial role of ERO1 $\alpha$  in tumor progression and treatment has been illustrated in many

types of human cancers [49–54]. For example, Zhang and colleagues reported that ERO1 $\alpha$  was significantly over-expressed and promoted cell proliferation and tumor growth in pancreatic ductal adenocarcinoma (PDAC) [49]. Tanaka et al. illustrated that ERO1 $\alpha$  levels were related to the number of blood vessels in triple-negative

breast cancer (TNBC) samples. Moreover, the expression of ERO1 $\alpha$  promoted tumor growth by augmenting angiogenesis [53]. Our findings correlate with the results of previous studies, suggesting that ERO1 $\alpha$  is critical for cell proliferation and angiogenesis and unveiling a new molecular link between mTORC1 activation and tumor development. Because aberrations in the PI3K/AKT/mTORC1 pathway are common in PDAC and TNBC [55, 56], it is likely that hyperactivated mTORC1 in these cancers upregulates ERO1 $\alpha$  expression and then promotes tumor progression. In line with this, inhibition of mTORC1 led to a significantly downregulated expression of ERO1 $\alpha$  in the PDAC cells PANC-1 and the breast cancer cells MDA-MB-231 (Supplementary Fig. 8C, D). Therefore, ERO1 $\alpha$  is a potential therapeutic target for mTORC1-related cancers.

Inducing ferroptosis in tumor cells has promising potential for cancer treatment, but its regulatory networks remain largely unclear. ERO1 $\alpha$  is an endoplasmic reticulum (ER) stress-related gene, which improves cell perseverance against challenges of high levels of protein misfolding during ER stress by retaining the good activity of oxidative protein folding [49, 50, 57]. In this study, in addition to accelerating cell proliferation and promoting angiogenesis, we found that ERO1 $\alpha$  plays a critical role in ferroptosis resistance driven by mTORC1 based on the following evidence. First, knockout or knockdown of ERO1 $\alpha$  accelerated erastin-induced lipid peroxidation and ferroptotic death in mTORC1-activated cells, while overexpression of ERO1 $\alpha$  attenuated ferroptosis triggered by erastin in control cells. Second, the anti-ferroptosis role of ERO1 $\alpha$  was further confirmed by the observation that inhibition of ferroptosis using Lip-1 partly rescued ERO1 $\alpha$  depletion-mediated suppression of tumor growth and upregulation of MDA. Therefore, in addition to relieving ER stress caused by the massive synthesis of new proteins due to mTORC1 activation [58], elevated ERO1 $\alpha$  can protect mTORC1-activated cells against ferroptosis. Furthermore, through integration analysis of RNA-seq data and subsequent functional validation, we found that elevated ERO1 $\alpha$  promotes ferroptosis resistance through upregulation of SLC7A11 in response to mTORC1 activation. This discovery confirmed the previous findings that SLC7A11 is critical for mTORC1-mediated glutathione synthesis [59] and unveiled a novel upstream regulator of SLC7A11. Thus, it is vital to sensitize mTORC1-activated cells to ferroptosis inducers by targeting this newly discovered ERO1 $\alpha$ /SLC7A11 pathway. In line with this, we showed that targeting ERO1 $\alpha$ , combined with the ferroptosis inducer IKE, has an excellent antitumor effect in three mTORC1-activated models, including NTC/T1 null cell xenografts, LSCC organoids, and LSCC PDX models. Therefore,

ERO1 $\alpha$  inhibition combined with ferroptosis induction constitutes a new and effective therapeutic strategy for some mTORC1-related cancers.

Angiogenesis, one of the hallmarks of cancer, facilitates tumor growth by playing a critical role in the delivery of oxygen and nutrients [60]. Previous studies have demonstrated that ERO1 $\alpha$  is involved in tumor angiogenesis. To date, the angiogenesis-promoting effects of ERO1 $\alpha$  have been linked to increased expression and secretion of vascular endothelial growth factor [51, 53, 61, 62]. In addition to ferroptosis resistance and cell proliferation, we propose here that ERO1 $\alpha$  also at least partially promotes angiogenesis via upregulation of SLC7A11 in mTORC1-activated cells. To our knowledge, this is the first report of direct evidence supporting SLC7A11 with the function of promoting angiogenesis. In addition, these findings provide a mechanistic explanation for a previous observation that administration of the SLC7A11 inhibitor erastin diminished angiogenesis in glioma [63]. However, it has not been investigated whether the angiogenesis-promoting effect of SLC7A11 depends on or is independent of its downstream GSH/GPX4 pathway. Future studies need to explore this issue.

Because SLC7A11 is frequently overexpressed in human malignancies and plays a significant role in ferroptosis resistance and tumor progression [64], it is critical to explore how SLC7A11 expression is controlled. An increasing number of studies suggest that the expression of SLC7A11 is finely regulated at the transcription level by transcription factors, at the post-transcription level by RNA binding proteins or noncoding RNAs, and at the protein degradation level by proteasome [59, 65–73]. In this study, we illustrated that ERO1 $\alpha$  stimulates STAT3 activity through upregulation of IL-6. Subsequently, activated STAT3 promotes the transcription of SLC7A11 by directly binding with the promoter of the *SLC7A11* gene. We identified IL-6 as a novel target of ERO1 $\alpha$  and confirmed the suggestion by previous studies conducted using other cancer cell models that STAT3 directly transcriptional regulates SLC7A11 [74, 75]. In addition, this may help to explain why IL-6 is elevated in mTORC1-related tumors. For example, IL-6 is significantly upregulated and plays a critical role in the development of tuberous sclerosis complex, a benign tumor syndrome caused by aberrant mTORC1 activation due to the loss of either TSC1 or TSC2 [76]. Considering our findings, overactivated mTORC1 likely facilitates the expression of IL-6 through upregulation of ERO1 $\alpha$ , thus promoting cell proliferation and tumor growth in the TSC. Interestingly, it has also been reported that STAT3 upregulates SLC7A11 through p53 downregulation, thus alleviating p53-mediated transcriptional inhibition of SLC7A11 [77]. This scenario could be ruled out because the

Tsc2<sup>-/-</sup> MEFs used here were p53 null. Furthermore, a limitation of this study is that the cytokine antibody array kit we used only covers 40 common cytokines. Investigating whether other cytokines are also involved in ERO1 $\alpha$ -mediated upregulation of SLC7A11 in the future would be interesting. Furthermore, it is worth exploring whether ERO1 $\alpha$  directly affects the formation of disulfide bonds in SLC7A11, thereby affecting its expression level and activity.

In summary, we have demonstrated that aberrantly activated mTORC1 contributes to ferroptosis resistance and tumor growth by regulating of the ERO1 $\alpha$ /IL-6/STAT3/SLC7A11 signaling pathway (Fig. 8M). Our findings will help in the elucidation of the molecular mechanism by which dysregulated mTORC1 signaling drives resistance to ferroptosis and tumorigenesis, indicating that combining ERO1 $\alpha$  inhibition with ferroptosis inducers may be a novel therapeutic strategy for the treatment of mTORC1-related tumors.

#### Abbreviations

mTOR	Mechanistic target of rapamycin
mTORC1	Mammalian target of rapamycin complex 1
mTORC2	Mechanistic target of rapamycin complex 2
TSC1	Tuberous sclerosis 1
TSC2	Tuberous sclerosis 2
Rheb	Ras homologue enriched in brain
AKT	Protein kinase B
GSH	Glutathione
L-ROS	Lipid reactive oxygen species
MDA	Malondialdehyde
GPX4	Glutathione peroxidase 4
SLC7A11	Solute carrier family 7 member 11
Lip-1	Lipoxystatin-1
MEFs	Mouse embryonic fibroblasts
LSCC	Laryngeal squamous cell carcinoma
PDO	Patient-derived Organoid
PDX	Patient-derived xenograft
ERO1 $\alpha$	Endoplasmic reticulum oxidoreductase 1 alpha
IL-6	Interleukin-6
STAT3	Signal transducer and activator of transcription 3
RSL3	RAS-selective lethal 3
IKE	Imidazole ketone erastin
DFX	Deferoxamine
MIG	Monokine induced by interferon-gamma
MIP-1 $\alpha$	Macrophage inflammatory protein-1alpha
HUVECs	Human umbilical vein endothelial cells
HEK 293T	Human embryonic kidney 293T
ANM	Adjacent normal tissues
qRT-PCR	Quantitative real-time PCR
IF	Immunofluorescence
TEM	Transmission electron microscopy
ChIP	Chromatin immunoprecipitation
CCK-8	Cell Counting Kit-8
CAM	Chicken chorioallantoic membrane
ELISA	Enzyme-linked immunosorbent assay
IHC	Immunohistochemistry
ELT3	Tsc2-null rat uterine leiomyoma cells
hiPSCs	Human induced pluripotent stem cells
HK2	Hexokinase
ENO3	Enolase 3
siRNAs	Small interfering RNA
HIF-1 $\alpha$	Hypoxia-inducible factor-1
shRNA	Short hairpin RNA

DEGs	Differentially expressed genes
4-HNE	4-Hydroxynonenal
PDAC	Pancreatic ductal adenocarcinoma
TNBC	Triple-negative breast cancer

#### Supplementary Information

The online version contains supplementary material available at <https://doi.org/10.1186/s13046-024-03039-2>.

##### Supplementary Material 1.

##### Supplementary Material 2.

##### Supplementary Material 3.

##### Supplementary Material 4.

##### Supplementary Material 5.

#### Authors' contributions

XJZ, SMZ and YHL supervised the project; XJZ, SMZ and DPL designed the experiments; ZXW, HYZ, WWL, WL, AJS, ZD, XC, XFW, YYL, ZDH and HWL performed the experiments; ZXW, HYZ and WL analyzed the data; XJZ, ZXW, and WWL wrote the paper; XJZ, DPL, WL and HBZ revised the paper. All authors read and approved the manuscript.

#### Funding

This work was supported by Anhui Provincial Natural Science Foundation (2208085MH239), the Natural Science Foundation of China (81372475, 82171127, and 82303021), the Natural Science Foundation of Universities of Anhui Province (KJ2019A0219), Discipline Construction Project of the First Affiliated Hospital of Anhui Medical University (No. 4245), Basic and Clinical Cooperative Research Promotion Program of Anhui Medical University (2023xkjT024), Anhui Medical University Affiliated Bozhou Hospital Talent Introduction Research Initiation Fund (by2023058), the ASHIPS Director's Fund (YZJJ2022QN48) and Postgraduate Innovation Research and Practice Program of Anhui Medical University (YJS20230027).

#### Availability of data and materials

All data generated and analyzed during this study are included in this published article and supplementary information. Materials generated during the present study are available from the corresponding author on reasonable request. The GEO accession number for RNA-seq data is GSE246899.

#### Declarations

##### Ethics approval and consent to participate

The collection of clinical samples in this study was carried out in accordance with the requirements of the Research Ethics Committee of the First Affiliated Hospital of Anhui Medical University (PJ 2021–02-32), and all patients signed informed consent. All animal experiments were carried out in accordance with the requirements of the Experimental Animal Ethical Committee of Anhui Medical University (LLSC-20211080).

##### Consent for publication

All authors have agreed to publish this manuscript.

##### Competing interests

The authors have no conflict of interests to declare.

##### Author details

<sup>1</sup>Department of Biochemistry & Molecular Biology, School of Basic Medicine, Anhui Medical University, No. 81 Meishan Road, Hefei 230032, Anhui Province, China. <sup>2</sup>Department of Otorhinolaryngology, Head & Neck Surgery, The First Affiliated Hospital of Anhui Medical University, Hefei 230022, China. <sup>3</sup>Department of Stomatology, The First Affiliated Hospital of Anhui Medical University, Hefei 230022, China. <sup>4</sup>Hefei Cancer Hospital, Chinese Academy of Sciences, Hefei 230031, China. <sup>5</sup>Department of Thyroid and Breast Surgery, Hefei First People's Hospital, Hefei 230061, China. <sup>6</sup>Modern Research Center for Traditional Chinese Medicine, Beijing Research Institute of Chinese Medicine,



Beijing University of Chinese Medicine, Beijing 100029, China. <sup>7</sup>State Key Laboratory of Medical Molecular Biology, Department of Physiology, Institute of Basic Medical Sciences and School of Basic Medicine, Peking Union Medical College and Chinese Academy of Medical Sciences, Beijing 100730, China. <sup>8</sup>Anhui Public Health Clinical Center, Hefei 230011, China. <sup>9</sup>Department of Otorhinolaryngology, Head & Neck Surgery, The Affiliated Bozhou Hospital of Anhui Medical University, No. 616 Duzhong Road, Bozhou 236800, Anhui Province, China. <sup>10</sup>Children's Hospital of Fudan University, National Children's Medical Center, And Institutes of Biomedical Sciences, Fudan University, Shanghai 200032, China.

Received: 1 January 2024 Accepted: 8 April 2024  
Published online: 13 April 2024

## References

- Battaglioni S, Benjamin D, Wälchli M, Maier T, Hall MN. mTOR substrate phosphorylation in growth control. *Cell*. 2022;185:1814–36.
- Liu GY, Sabatini DM. mTOR at the nexus of nutrition, growth, ageing and disease. *Nat Rev Mol Cell Biol*. 2020;21:183–203.
- Goul C, Peruzzo R, Zoncu R. The molecular basis of nutrient sensing and signalling by mTORC1 in metabolism regulation and disease. *Nat Rev Mol Cell Biol*. 2023;24:857–75.
- Valvezan AJ, Manning BD. Molecular logic of mTORC1 signalling as a metabolic rheostat. *Nat Metab*. 2019;1:321–33.
- Kim J, Guan KL. mTOR as a central hub of nutrient signalling and cell growth. *Nat Cell Biol*. 2019;21:63–71.
- Yu L, Wei J, Liu P. Attacking the PI3K/Akt/mTOR signaling pathway for targeted therapeutic treatment in human cancer. *Semin Cancer Biol*. 2022;85:69–94.
- Luo C, Ye WR, Shi W, Yin P, Chen C, He YB, Chen MF, Zu XB, Cai Y. Perfect match: mTOR inhibitors and tuberous sclerosis complex. *Orphanet J Rare Dis*. 2022;17:106.
- Popova NV, Jücker M. The role of mTOR signaling as a therapeutic target in cancer. *Int J Mol Sci*. 2021;22:1743.
- Glaviano A, Foo ASC, Lam HY, Yap KCH, Jacot W, Jones RH, Eng H, Nair MG, Makvandi P, Georger B, et al. PI3K/AKT/mTOR signaling transduction pathway and targeted therapies in cancer. *Mol Cancer*. 2023;22:138.
- Stockwell BR. Ferroptosis turns 10: emerging mechanisms, physiological functions, and therapeutic applications. *Cell*. 2022;185:2401–21.
- Rochette L, Dogon G, Rigal E, Zeller M, Cottin Y, Vergely C. Lipid peroxidation and iron metabolism: two corner stones in the homeostasis control of ferroptosis. *Int J Mol Sci*. 2022;24:449.
- Ayala A, Muñoz MF, Argüelles S. Lipid peroxidation: production, metabolism, and signaling mechanisms of malondialdehyde and 4-hydroxy-2-nonenal. *Oxid Med Cell Longev*. 2014;2014:360438.
- Dixon SJ, Pratt DA. Ferroptosis: a flexible constellation of related biochemical mechanisms. *Mol Cell*. 2023;83:1030–42.
- Wang X, Zhou Y, Min J, Wang F. Zooming in and out of ferroptosis in human disease. *Front Med*. 2023;17:173–206.
- Jiang X, Stockwell BR, Conrad M. Ferroptosis: mechanisms, biology and role in disease. *Nat Rev Mol Cell Biol*. 2021;22:266–82.
- Tang D, Chen X, Kang R, Kroemer G. Ferroptosis: molecular mechanisms and health implications. *Cell Res*. 2021;31:107–25.
- Du Y, Guo Z. Recent progress in ferroptosis: inducers and inhibitors. *Cell Death Discov*. 2022;8:501.
- Wang Y, Wu X, Ren Z, Li Y, Zou W, Chen J, Wang H. Overcoming cancer chemotherapy resistance by the induction of ferroptosis. *Drug Resist Updat*. 2023;66:100916.
- Lei G, Zhuang L, Gan B. Targeting ferroptosis as a vulnerability in cancer. *Nat Rev Cancer*. 2022;22:381–96.
- Lei G, Zhuang L, Gan B. mTORC1 and ferroptosis: regulatory mechanisms and therapeutic potential. *BioEssays*. 2021;43:e2100093.
- Zhang Y, Swanda RV, Nie L, Liu X, Wang C, Lee H, Lei G, Mao C, Koppula P, Cheng W, et al. mTORC1 couples cyst(e)ine availability with GPX4 protein synthesis and ferroptosis regulation. *Nat Commun*. 2021;12:1589.
- Yi J, Zhu J, Wu J, Thompson CB, Jiang X. Oncogenic activation of PI3K-AKT-mTOR signaling suppresses ferroptosis via SREBP-mediated lipogenesis. *Proc Natl Acad Sci U S A*. 2020;117:31189–97.
- Li H, Liu P, Li D, Wang Z, Ding Z, Zhou M, Chen X, Miao M, Ding J, Lin W, et al. STAT3/miR-130b-3p/MBNL1 feedback loop regulated by mTORC1 signaling promotes angiogenesis and tumor growth. *J Exp Clin Cancer Res*. 2022;41:297.
- Zha X, Wang F, Wang Y, He S, Jing Y, Wu X, Zhang H. Lactate dehydrogenase B is critical for hyperactive mTOR-mediated tumorigenesis. *Cancer Res*. 2011;71:13–8.
- Li D, Sun A, Zhang L, Ding Z, Yi F, Yang X, Wang Z, Chen X, Liu W, Liu S, et al. Elevated ITGA5 facilitates hyperactivated mTORC1-mediated progression of laryngeal squamous cell carcinoma via upregulation of EFNB2. *Theranostics*. 2022;12:7431–49.
- Chen X, Miao M, Zhou M, Chen J, Li D, Zhang L, Sun A, Guan M, Wang Z, Liu P, et al. Poly-L-arginine promotes asthma angiogenesis through induction of FGFBP1 in airway epithelial cells via activation of the mTORC1-STAT3 pathway. *Cell Death Dis*. 2021;12:761.
- Ma J, Meng Y, Kwiatkowski DJ, Chen X, Peng H, Sun Q, Zha X, Wang F, Wang Y, Jing Y, et al. Mammalian target of rapamycin regulates murine and human cell differentiation through STAT3/p63/Jagged/Notch cascade. *J Clin Invest*. 2010;120:103–14.
- Driehuis E, Kolders S, Spelier S, Löhmußaar K, Willems SM, Devriese LA, de Bree R, de Ruiter EJ, Korving J, Begthel H, et al. Oral mucosal organoids as a potential platform for personalized cancer therapy. *Cancer Discov*. 2019;9:852–71.
- Hu Z, Wang Y, Huang F, Chen R, Li C, Wang F, Goto J, Kwiatkowski DJ, Wdziecak-Bakala J, Tu P, et al. Brain-expressed X-linked 2 Is pivotal for hyperactive mechanistic target of rapamycin (mTOR)-mediated tumorigenesis. *J Biol Chem*. 2015;290:25756–65.
- Chang JW, Zhang W, Yeh HS, de Jong EP, Jun S, Kim KH, Bae SS, Beckman K, Hwang TH, Kim KS, et al. mRNA 3'-UTR shortening is a molecular signature of mTORC1 activation. *Nat Commun*. 2015;6:7218.
- Shrestha S, Lamattina A, Pacheco-Rodriguez G, Ng J, Liu X, Sonawane A, Imani J, Qiu W, Kosmas K, Louis P, et al. ETV2 regulates PARP-1 binding protein to induce ER stress-mediated death in tuberin-deficient cells. *Life Sci Alliance*. 2022;5:e202201369.
- Hernandez JOR, Wang X, Vazquez-Segoviano M, Lopez-Marfil M, Sobral-Reyes MF, Moran-Horowich A, Sundberg M, Lopez-Cantu DO, Probst CK, Ruiz-Esparza GU, et al. A tissue-bioengineering strategy for modeling rare human kidney diseases in vivo. *Nat Commun*. 2021;12:6496.
- Li C, Chen H, Lan Z, He S, Chen R, Wang F, Liu Z, Li K, Cheng L, Liu Y, et al. mTOR-dependent upregulation of xCT blocks melanin synthesis and promotes tumorigenesis. *Cell Death Differ*. 2019;26:2015–28.
- Ciscato F, Ferrone L, Masgras I, Laquatra C, Rasola A. Hexokinase 2 in cancer: a prima donna playing multiple characters. *Int J Mol Sci*. 2021;22:4716.
- Fortunato S, Bononi G, Granchi C, Minutolo F. An update on patents covering agents that interfere with the cancer glycolytic cascade. *ChemMedChem*. 2018;13:2251–65.
- Szwed A, Kim E, Jacinto E. Regulation and metabolic functions of mTORC1 and mTORC2. *Physiol Rev*. 2021;101:1371–426.
- Kajiwaru T, Tanaka T, Kukita K, Kutomi G, Saito K, Okuya K, Takaya A, Kochin V, Kanaseki T, Tsukahara T, et al. Hypoxia augments MHC class I antigen presentation via facilitation of ERO1- $\alpha$ -mediated oxidative folding in murine tumor cells. *Eur J Immunol*. 2016;46:2842–51.
- Laplanche M, Sabatini DM. mTOR signaling at a glance. *J Cell Sci*. 2009;122:3589–94.
- Zhang H, Bajraszewski N, Wu E, Wang H, Moseman AP, Dabora SL, Griffin JD, Kwiatkowski DJ. PDGFRs are critical for PI3K/Akt activation and negatively regulated by mTOR. *J Clin Invest*. 2007;117:730–8.
- Shergalis AG, Hu S, Bankhead A 3rd, Neamati N. Role of the ERO1-PDI interaction in oxidative protein folding and disease. *Pharmacol Ther*. 2020;210:107525.
- Jha V, Kumari T, Manickam V, Assar Z, Olson KL, Min JK, Cho J. ERO1-PDI redox signaling in health and disease. *Antioxid Redox Signal*. 2021;35:1093–115.
- Huang B, Lang X, Li X. The role of IL-6/JAK2/STAT3 signaling pathway in cancers. *Front Oncol*. 2022;12:1023177.
- Zhang Y, Tan H, Daniels JD, Zandkarimi F, Liu H, Brown LM, Uchida K, O'Connor OA, Stockwell BR. Imidazole ketone erastin induces ferroptosis and slows tumor growth in a mouse lymphoma model. *Cell Chem Biol*. 2019;26:623–633.e629.

44. Wang E, Xiang K, Zhang Y, Wang X-F. Patient-derived organoids (PDOs) and PDO-derived xenografts (PDOXs): new opportunities in establishing faithful pre-clinical cancer models. *J Natl Cancer Cent.* 2022;2:263–76.
45. Mao B, Zhang Q, Ma L, Zhao DS, Zhao P, Yan P. Overview of research into mTOR inhibitors. *Molecules.* 2022;27:5295.
46. Sun SY. mTOR-targeted cancer therapy: great target but disappointing clinical outcomes, why? *Front Med.* 2021;15:221–31.
47. Ali ES, Mitra K, Akter S, Ramproshad S, Mondal B, Khan IN, Islam MT, Sharifi-Rad J, Calina D, Cho WC. Recent advances and limitations of mTOR inhibitors in the treatment of cancer. *Cancer Cell Int.* 2022;22:284.
48. Takei N, Yoneda A, Kosaka M, Sakai-Sawada K, Tamura Y. ERO1 $\alpha$  is a novel endogenous marker of hypoxia in human cancer cell lines. *BMC Cancer.* 2019;19:510.
49. Zhang J, Yang J, Lin C, Liu W, Huo Y, Yang M, Jiang SH, Sun Y, Hua R. Endoplasmic reticulum stress-dependent expression of ero1l promotes aerobic glycolysis in pancreatic cancer. *Theranostics.* 2020;10:8400–14.
50. Liu L, Li S, Qu Y, Bai H, Pan X, Wang J, Wang Z, Duan J, Zhong J, Wan R, et al. Ablation of ERO1A induces lethal endoplasmic reticulum stress responses and immunogenic cell death to activate anti-tumor immunity. *Cell Rep Med.* 2023;4:101206.
51. Varone E, Decio A, Chernorudskiy A, Minoli L, Brunelli L, Ioli F, Piotti A, Pastorelli R, Fratelli M, Gobbi M, et al. The ER stress response mediator ERO1 triggers cancer metastasis by favoring the angiogenic switch in hypoxic conditions. *Oncogene.* 2021;40:1721–36.
52. Lei Y, Zhang R, Lu Z, Zhang G, Huang J, Liu C, Wang Z, Mao S, Che Y, Wang X, et al. ERO1L promotes IL6/sIL6R signaling and regulates MUC16 expression to promote CA125 secretion and the metastasis of lung cancer cells. *Cell Death Dis.* 2020;11:853.
53. Tanaka T, Kutomi G, Kajiwara T, Kukita K, Kochin V, Kanaseki T, Tsukahara T, Hirohashi Y, Torigoe T, Okamoto Y, et al. Cancer-associated oxidoreductase ERO1- $\alpha$  drives the production of VEGF via oxidative protein folding and regulating the mRNA level. *Br J Cancer.* 2016;114:1227–34.
54. Chen P, Sharma A, Weiher H, Schmidt-Wolf IGH. Biological mechanisms and clinical significance of endoplasmic reticulum oxidoreductase 1 alpha (ERO1 $\alpha$ ) in human cancer. *J Exp Clin Cancer Res.* 2024;43:71.
55. Mortazavi M, Moosavi F, Martini M, Giovannetti E, Firuzi O. Prospects of targeting PI3K/AKT/mTOR pathway in pancreatic cancer. *Crit Rev Oncol Hematol.* 2022;176:103749.
56. Costa RLB, Han HS, Gradishar WJ. Targeting the PI3K/AKT/mTOR pathway in triple-negative breast cancer: a review. *Breast Cancer Res Treat.* 2018;169:397–406.
57. Bassot A, Chen J, Takahashi-Yamashiro K, Yap MC, Gibhardt CS, Le GNT, Hario S, Nasu Y, Moore J, Gutiérrez T, et al. The endoplasmic reticulum kinase PERK interacts with the oxidoreductase ERO1 to metabolically adapt mitochondria. *Cell Rep.* 2023;42:111899.
58. Dong G, Liu Y, Zhang L, Huang S, Ding HF, Dong Z. mTOR contributes to ER stress and associated apoptosis in renal tubular cells. *Am J Physiol Renal Physiol.* 2015;308:F267–274.
59. Torrence ME, MacArthur MR, Hosios AM, Valvezan AJ, Asara JM, Mitchell JR, Manning BD. The mTORC1-mediated activation of ATF4 promotes protein and glutathione synthesis downstream of growth signals. *Elife.* 2021;10:e63326.
60. Viallard C, Larrivée B. Tumor angiogenesis and vascular normalization: alternative therapeutic targets. *Angiogenesis.* 2017;20:409–26.
61. Varone E, Chernorudskiy A, Cherubini A, Cattaneo A, Bachi A, Fumagalli S, Erol G, Gobbi M, Lenardo MJ, Borgese N, Zito E. ERO1 alpha deficiency impairs angiogenesis by increasing N-glycosylation of a proangiogenic VEGFA. *Redox Biol.* 2022;56:102455.
62. Yang S, Yang C, Yu F, Ding W, Hu Y, Cheng F, Zhang F, Guan B, Wang X, Lu L, Rao J. Endoplasmic reticulum resident oxidase ERO1-L $\alpha$  promotes hepatocellular carcinoma metastasis and angiogenesis through the S1PR1/STAT3/VEGF-A pathway. *Cell Death Dis.* 2018;9:1105.
63. Chen D, Fan Z, Rauh M, Buchfelder M, Eyupoglu IY, Savaskan N. ATF4 promotes angiogenesis and neuronal cell death and confers ferroptosis in a xCT-dependent manner. *Oncogene.* 2017;36:5593–608.
64. Koppula P, Zhuang L, Gan B. Cystine transporter SLC7A11/xCT in cancer: ferroptosis, nutrient dependency, and cancer therapy. *Protein Cell.* 2021;12:599–620.
65. Jiang L, Kon N, Li T, Wang SJ, Su T, Hibshoosh H, Baer R, Gu W. Ferroptosis as a p53-mediated activity during tumour suppression. *Nature.* 2015;520:57–62.
66. Li Y, Yang W, Zheng Y, Dai W, Ji J, Wu L, Cheng Z, Zhang J, Li J, Xu X, et al. Targeting fatty acid synthase modulates sensitivity of hepatocellular carcinoma to sorafenib via ferroptosis. *J Exp Clin Cancer Res.* 2023;42:6.
67. Drayton RM, Dudzic E, Peter S, Bertz S, Hartmann A, Bryant HE, Catto JW. Reduced expression of miRNA-27a modulates cisplatin resistance in bladder cancer by targeting the cystine/glutamate exchanger SLC7A11. *Clin Cancer Res.* 2014;20:1990–2000.
68. Zhang B, Bao W, Zhang S, Chen B, Zhou X, Zhao J, Shi Z, Zhang T, Chen Z, Wang L, et al. LncRNA HEPFAL accelerates ferroptosis in hepatocellular carcinoma by regulating SLC7A11 ubiquitination. *Cell Death Dis.* 2022;13:734.
69. Chen Q, Zheng W, Guan J, Liu H, Dan Y, Zhu L, Song Y, Zhou Y, Zhao X, Zhang Y, et al. SOCS2-enhanced ubiquitination of SLC7A11 promotes ferroptosis and radiosensitization in hepatocellular carcinoma. *Cell Death Differ.* 2023;30:137–51.
70. Liu T, Jiang L, Tavara O, Gu W. The deubiquitylase OTUB1 mediates ferroptosis via stabilization of SLC7A11. *Cancer Res.* 2019;79:1913–24.
71. Zhang W, Sun Y, Bai L, Zhi L, Yang Y, Zhao Q, Chen C, Qi Y, Gao W, He W, et al. RBMS1 regulates lung cancer ferroptosis through translational control of SLC7A11. *J Clin Invest.* 2021;131:e152067.
72. Wang X, Chen Y, Wang X, Tian H, Wang Y, Jin J, Shan Z, Liu Y, Cai Z, Tong X, et al. Stem cell factor SOX2 confers ferroptosis resistance in lung cancer via upregulation of SLC7A11. *Cancer Res.* 2021;81:5217–29.
73. Yang J, Zhou Y, Xie S, Wang J, Li Z, Chen L, Mao M, Chen C, Huang A, Chen Y, et al. Metformin induces ferroptosis by inhibiting UFMylation of SLC7A11 in breast cancer. *J Exp Clin Cancer Res.* 2021;40:206.
74. Ouyang S, Li H, Lou L, Huang Q, Zhang Z, Mo J, Li M, Lu J, Zhu K, Chu Y, et al. Inhibition of STAT3-ferroptosis negative regulatory axis suppresses tumor growth and alleviates chemoresistance in gastric cancer. *Redox Biol.* 2022;52:102317.
75. Li M, Jin S, Zhang Z, Ma H, Yang X. Interleukin-6 facilitates tumor progression by inducing ferroptosis resistance in head and neck squamous cell carcinoma. *Cancer Lett.* 2022;527:28–40.
76. Wang J, Filippakis H, Hougard T, Du H, Ye C, Liu HJ, Zhang L, Hindi K, Bagwe S, Nijmeh J, et al. Interleukin-6 mediates PSAT1 expression and serine metabolism in TSC2-deficient cells. *Proc Natl Acad Sci U S A.* 2021;118:e2101268118.
77. Li X, Qi H, Zhang X, Liang H, Zeng N. Jing-Fang n-butanol extract and its isolated JFNE-C inhibit ferroptosis and inflammation in LPS induced RAW264.7 macrophages via STAT3/p53/SLC7A11 signaling pathway. *J Ethnopharmacol.* 2023;316:116689.

## Publisher's Note

Springer Nature remains neutral with regard to jurisdictional claims in published maps and institutional affiliations.